Technical Report Documentation Page

1. Report No. FHWA/TX-09/0-4893-4	2. Government Accession No.	3. Recipient's Catalog No.
4. Title and Subtitle Debonding in Bonded Concrete Overlays over Continuously Reinforced Concrete Pavements		5. Report Date June 2008 6. Performing Organization Code
7. Author(s) Lucas Lahitou, Seong-Cheol Choi, and Moon Won		8. Performing Organization Report No. 0-4893-4
9. Performing Organization Name and Address Center for Transportation Research The University of Texas at Austin 3208 Red River, Suite 200 Austin, TX 78705-2650		10. Work Unit No. (TRAIS) 11. Contract or Grant No. 0-4893
12. Sponsoring Agency Name and Address Texas Department of Transportation Research and Technology Implementation Office P.O. Box 5080 Austin, TX 78763-5080		13. Type of Report and Period Covered Technical Report, 2006-2007 14. Sponsoring Agency Code

15. Supplementary Notes
Project performed in cooperation with the Texas Department of Transportation and the Federal Highway Administration.

16. Abstract

Field evaluations of bonded concrete overlay (BCO) performance reveal that debonding between old and new concrete is responsible for distresses in BCO. An in-depth investigation is needed to fully understand debonding mechanisms and their effects on distresses in BCO. A literature review conducted as part of this study revealed that, although most currently available BCO design procedures recognize the importance of attaining a perfect bond between the overlay and the substrate, they do not address this aspect directly. Therefore, this study is aimed at investigating the mechanics of debonding under environmental loading at early ages and, based on an evaluation of these mechanisms, at developing a model capable of determining the extent of debonding for a variety of material, structural and environmental conditions. To that end, two 2-dimensional finite element models were developed. These models characterize debonding from the perspective of reflective cracks and non-reflective (top-down) cracks. The evaluation of analysis results demonstrates that the most critical scenario is debonding in non-reflective cracks. Next, the behavior of BCO was investigated through sensitivity analysis. The non-reflective crack debonding model is sensitive to slab thickness, modulus, and CTE of overlay concrete and the interface bond strength. All the other variables included in the analysis, including slab thickness and CTE of existing concrete slab had little effect on debonding.

17. Key Words	18. Distribution Statement
Delamination, debonding, bonding concrete overlay (BCO), asphalt concrete overlay (ACO), life cycle cost analysis (LCCA)	No restrictions. This document is available to the public through the National Technical Information Service, Springfield, Virginia 22161; www.ntis.gov.

19. Security Classif. (of report)	20. Security Classif. (of this page)	21. No. of pages	22. Price
Unclassified	Unclassified	66	

Form DOT F 1700.7 (8-72) Reproduction of completed page authorized

DEBONDING IN BONDED CONCRETE OVERLAYS OVER CONTINUOUSLY REINFORCED CONCRETE PAVEMENTS

Lucas Lahitou
Seong-Cheol Choi
Moon Won

CTR Technical Report:	0-4893-4
Report Date:	June 2008
Project:	0-4893
Project Title:	Performance of Old Concrete Under Thin Overlays
Sponsoring Agency:	Texas Department of Transportation
Performing Agency:	Center for Transportation Research at The University of Texas at Austin

Project performed in cooperation with the Texas Department of Transportation and the Federal Highway Administration.

Center for Transportation Research
The University of Texas at Austin
3208 Red River
Austin, TX 78705

www.utexas.edu/research/ctr

Disclaimers

Author's Disclaimer: The contents of this report reflect the views of the authors, who are responsible for the facts and the accuracy of the data presented herein. The contents do not necessarily reflect the official view or policies of the Federal Highway Administration or the Texas Department of Transportation (TxDOT). This report does not constitute a standard, specification, or regulation.

Patent Disclaimer: There was no invention or discovery conceived or first actually reduced to practice in the course of or under this contract, including any art, method, process, machine manufacture, design or composition of matter, or any new useful improvement thereof, or any variety of plant, which is or may be patentable under the patent laws of the United States of America or any foreign country.

Engineering Disclaimer

NOT INTENDED FOR CONSTRUCTION, BIDDING, OR PERMIT PURPOSES.

Research Supervisor: Moon Won

Acknowledgments

The authors express their appreciation to the project director, Dr. German Claros. Valuable comments were received from the Project Monitoring Committee (PMC). Thanks to the district pavement engineers in the Bryan, Fort Worth, Houston, and Dallas districts and all TxDOT personnel that helped achieving the tasks throughout this project.

Table of Contents

List of Tables

List of Figures

Chapter 1. Introduction

1.1 Introduction

Concrete pavements are subject to traffic and environmental loading that will, over time, cause distress and result in the loss of structural and functional performance. In turn, the loss of pavement performance results in increased dissatisfaction among the traveling public and increased user and agency costs. Consequently, highway agencies need to implement timely and cost efficient techniques or procedures as means of reducing roughness or enhancing the structural capacity of existing pavements.

For rigid pavements, rehabilitation strategies often involve the application of Portland cement concrete (PCC) overlays over the surface of the existing pavement. Depending on the bond condition, PCC overlays can be classified into bonded, partially bonded or unbonded. Although both flexible and rigid overlays can be used to correct roughness and enhance the structural capacity of pavements, in recent years, focus has been placed on rehabilitation strategies that allow for longer service life and minimize life-cycle costs. In this context, resurfacing with a bonded concrete overlay (BCO), a rehabilitation procedure in which a layer of concrete is placed over the existing pavement to form a monolithic structure, has proven to be a cost-effective rehabilitation strategy [1]. However, field experience has shown that, under certain conditions, premature failures have occurred. A review of relevant literature documenting experimental rehabilitation projects provided insight into the possible causes that resulted in these premature failures. In most cases, these failures have been attributed to the debonding of the overlay from the existing pavement [2, 3, 4]. Based on follow-up studies investigating the mechanics of debonding, it is now known that debonding is an early-age phenomenon that generally occurs in the presence of adverse environmental conditions [5, 6, 7].

Throughout the last two decades, efforts have been made to develop more realistic mechanistic-empirical overlay design procedures. However, a literature review of the currently available BCO design methodologies conducted as part of this study revealed that, although most methods recognize the importance of attaining a good bond between the overlay and the substrate, they do not address this aspect directly.

Therefore, it is imperative that debonding be included as a distress mechanism for the design of BCOs. To that end, the purpose of this study is to investigate debonding mechanisms under environmental loading at early ages and, based on an evaluation of these mechanisms, to develop a mechanistic model capable of determining the extent of debonding for a variety of material, geometric and environmental conditions.

1.2 Scope

This study is primarily concerned with BCOs over continuously reinforced concrete pavements (CRCPs). Theoretical analysis of debonding mechanisms using a computer program constitutes the major portion of this study. Even though field validation of the results of the analysis is considered a vital part of any mechanistic-empirical pavement design procedures, field validation has not been conducted in this study.

1.3 Organization

In the pre-phase of this study, an extensive literature review was conducted to gather information regarding the long term structural behavior of BCOs. Current design practices and accounted failure mechanisms are summarized in Chapter 2. In addition, towards the end of the chapter, the major limitations of these various methods are discusses and critiqued.

Chapter 3 discusses the development of two 2-dimensional finite element models to investigate the debonding mechanisms under various environmental loading conditions at an early age using DIANA [18], a multi-purpose, commercially available finite element program.

Chapter 4 presents the results of a parametric study carried out with the developed models to evaluate the effect of material, geometric and environmental conditions.

Chapter 5 discusses the findings and conclusions made in this study, with recommendations for future work.

Chapter 2. Literature Review

2.1 Introduction

Chapter 2 serves as an introductory chapter to this report, providing the reader with background information regarding the design of BCOs. The chapter first reviews what constitutes failure in both new and rehabilitated CRCP. Next, the most important concepts regarding the design of BCOs are presented, followed by a discussion of some of the most widely used design procedures. Towards the end of the chapter, a critique of these design procedures is presented, with specific attention to the accounted failure mechanism in each design methodology.

2.2 Failure

There are two distinctive categories of pavement failure: functional failure and structural failure. Functional failure refers to that stage at which the pavement has become unsafe or uncomfortable for the user, therefore, failing to serve the purpose for which it was designed for. On the other hand, structural failure occurs when a pavement has reached a pre-defined level of distress. In general, as structural failures precede functional failures, for design purposes, pavement engineers are mostly concerned with the appearance of distress.

In dealing with distress in both new and rehabilitated CRCP, punchouts have been identified as the most common distress manifestation. Based on the Federal Highways Administration (FHWA) Distress Identification Manual for the Long Term Pavement Performance Program (LTPP) [9], punchouts can be defined as a structural failure in which a piece of slab bound by two closely spaced transverse cracks, a longitudinal fatigue crack, and the pavement edge, is loosened from the main body and displaced down into the supporting layers through the action of heavy traffic loading. An illustration of a typical CRCP punchout is presented in Figure 2.1.

Figure 2.1: Typical CRCP punchout distress
(Source: FHWA HRT-04-122, 2005, Figure 64)

2.3 General Considerations

The objective of the BCO design process is to develop a pavement structure that reduces the critical stresses due to wheel loading to an acceptable level. The reduction of critical stress is achieved by the increased slab thickness provided by the BCO. To accomplish these objectives, pavement engineers need to identify the overlay thickness that is appropriate for the future design traffic, material, geometric and environmental conditions. For thickness design purposes, most widely accepted design procedures make use of the effective thickness approach. This method states that the required thickness of the overlay is the difference between the thickness required for a new pavement and the effective thickness of the existing pavement, as indicated by Equation 1.

$$D_{BCO} = D_f - D_{eff} \tag{1}$$

Where D_{BCO} is the thickness of the overlay, D_f is the required thickness to carry the future traffic if the pavement was constructed new, and D_{eff} is the effective thickness of the existing pavement.

2.4 Current Design Practices

A variety of models have been used by various agencies for the design of overlays, ranging from the early purely empirical methods to the modern mechanistic-empirical methods. Currently available pavement design methods include those developed by the U.S. Army Corps of Engineers [10], the Portland Cement Association (PCA) [10], the American Association of State Highway and Transportation Officials (ASSHTO) [10, 11] and the Mechanistic-Empirical Pavement Design Guide developed under National Cooperative Highway Research Program (NCHRP) 1-37(A) [12, 13], referred to as MEPDG in this thesis. In the following sections, the basic concepts behind the aforementioned design methodologies will be presented.

2.4.1 U. S. Army Corps of Engineers

This design methodology, originally developed for the design of PCC overlays over PCC airport pavements, was developed using the effective thickness approach previously introduced. In this methodology, empirical coefficients were introduced into Equation 0 based on the results of full-scale traffic tests, leaving Equation (2) as:

$$(D_{OL})^n = (D_f)^n - (C \cdot D_e)^n \tag{2}$$

Where D_{OL} is the thickness of the overlay; D_e is the thickness of the existing pavement; D_f is the required thickness to carry the future traffic if the pavement was constructed new; n is a coefficient that takes the value of 2 for unbonded overlays, 1.4 for partially bonded overlays and 1 for bonded overlays; and C is a coefficient that takes into account the condition of the existing pavement at the time of the overlay. Suggested values for C are as follows:

C = 1.0	for existing pavements in good overall structural condition with little or no cracking;
C = 0.75	for existing pavements with initial transverse and corner cracking due to loading but without progressive structural distress or recent cracking;
C = 0.35	for existing pavements that are badly cracked or structurally shattered.

As it can be inferred from Equation (2), overlay thicknesses calculated for the unbonded or partially bonded cases are larger than those obtained for the bonded case. Moreover, the design equations for the case of bonded overlays over structurally sound concrete pavements (n = 1 and C = 1) imply that the concrete in the existing pavement has suffered no fatigue damage accumulation as a result of traffic or other factors.

2.4.2 PCA

The basic design concept adopted in PCA method is to provide an overlay system that is structurally equivalent to a new full-depth pavement placed on the same subbase and subgrade. The premise of structural equivalency is based on the comparison of the ratio of flexural stress to flexural strength at the bottom of the new full depth pavement and that at the bottom of the overlaid system, as shown in Figure 2.2. If the ratio at the bottom of the new full-depth pavement is equal to or greater than that of the overlaid pavement system, as indicated in Equation (3), the required fatigue life of the overlaid pavement system will be satisfied.

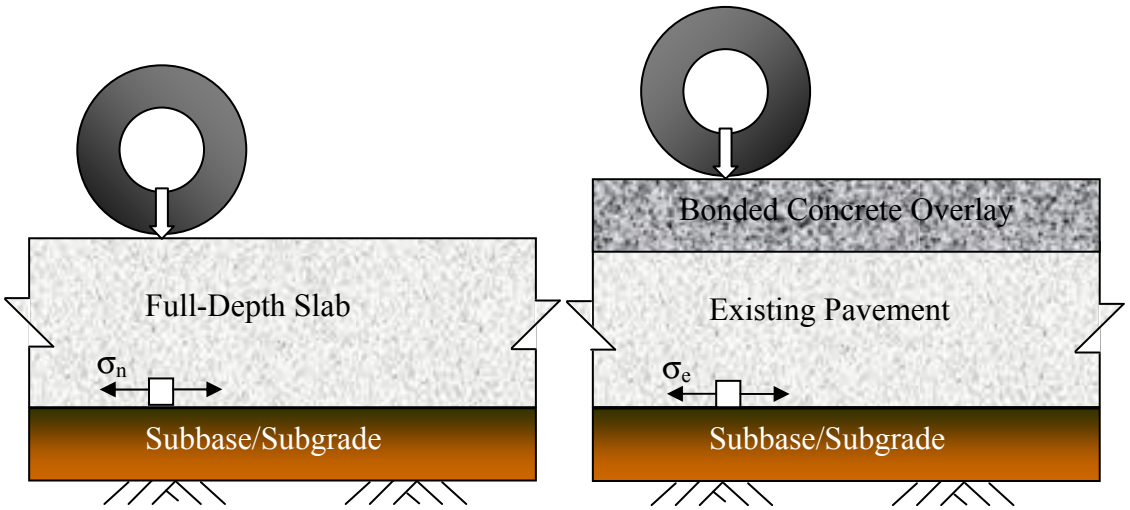

Figure 2.2: Edge stresses for new and overlaid pavement for PCA method design equivalency

$$\frac{\sigma_n}{S_{cn}} \geq \frac{\sigma_e}{S_{ce}} \tag{3}$$

where:

σ_n = critical edge stress in the new pavement

σ_e = critical edge stress in the existing pavement

S_{cn} = modulus of rupture of the new concrete

S_{ce} = modulus of rupture of the existing concrete

In addition, unlike the U.S. Army Corps of Engineers method, the remaining structural capacity of the existing pavement is directly taken into consideration in the design by means of a comprehensive evaluation of the existing pavement condition, which includes conducting pavement condition surveys, non-destructive deflection testing and in-situ material evaluation.

In developing this method, a finite element method program, JSLAB, was used to determine the tensile stress at the bottom of the new full depth pavement and the tensile stress at the bottom of the overlaid system for various different existing pavement conditions, characterized by the existing pavement flexural strength and support conditions. The computed stresses were then used to prepare the design chart shown in Figure 2.3. It should be noted that for the new concrete, the moduli of elasticity was assumed to be from 4 x 10^6 to 5 x 10^6 psi and the moduli of rupture from 600 to 650 psi. In the case of the existing pavement, the moduli of rupture from 526 to 575 psi, 476 to 525 psi, and 426 to 475 were used, as indicated by curve 1, curve 2 and curve 3 in the design chart, respectively. Moduli of elasticity for the existing concrete pavement were estimated using the following relationship:

$$E_C = D \cdot S_c \tag{4}$$

Where E_c is the modulus of elasticity of concrete in the existing pavement, S_c is the modulus of rupture of concrete in the existing pavement, and D is a coefficient that takes a value in the range of 6,000 to 7,000.

For cases when the modulus of rupture of the existing concrete is greater than 575psi, the existing pavement is considered to be as good as new, as indicated by the base line curve in the design chart, where the required thickness of the overlay can be computed as the difference between the new full depth slab pavement thickness and the existing pavement thickness.

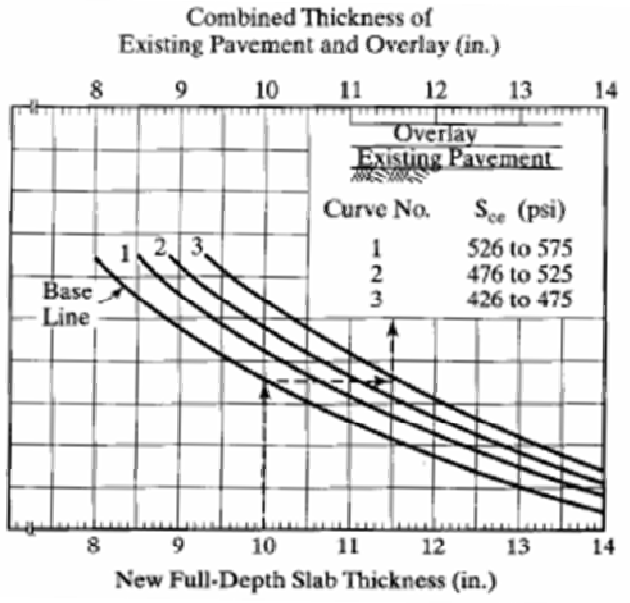

Figure 2.3: PCA bonded overlay design chart
(Source: Huang Y. H., 2004)

For design purposes, having calculated the required thickness to carry the future traffic (given the pavement was constructed new), the required overlay thickness can be determined by the application of the effective thickness approach, using the design chart presented above.

2.4.3 AASHTO

The AASHTO method, the most widely used design procedure among state agencies, was derived based on the analysis of data collected from the doweled jointed concrete pavement (JCP) sections from the AASHTO Road Test, and uses the effective thickness approach for design purposes. Similarly to the PCA method, the AASHTO method takes into consideration the remaining structural capacity of the existing pavement for the calculation of the effective thickness of the existing slab by the application of a condition factor (CF), as indicated by Equation (5).

$$D_{eff} = CF \times (D_e) \quad (5)$$

where:

D_{eff} = effective thickness of the existing pavement

CF = condition factor

D_e = thickness of the existing pavement

There are two methods for the determination of CF. One is by conducting condition surveys of the existing pavement, and the other is by considering the remaining life of the existing pavement. In the former method, visual distress surveys are conducted to provide the designer with data concerning the types of distress in the pavement, their location, severity and extension. According to AASHTO Design of Pavement Structures 1993 [11], distress types of to be recorded on CRCP sections are as follows:

(1) Number of punchouts per mile

(2) Number of deteriorated transverse cracks per mile

(3) Number of existing expansion joints, exceptionally wide joints (> 1 inch) or AC full depth patches

(4) Number of existing and new repairs prior to overlay per mile

(5) Presence and general severity of PCC durability problems

(6) Evidence of pumping of fines or water

Additional information about visual distress survey procedures and distress types can be found in Reference 9.

Having conducted the condition survey, the condition factor (CF) can be computed as the product of three adjustment factors, as follows:

$$CF = F_{jc} \times F_{dur} \times F_{fat} \quad (6)$$

where:

F_{jc} = joints and cracks adjustment factor

F_{dur} = durability adjustment factor

F_{fat} = fatigue damage adjustment factor

Where F_{jc} stands for joint and cracks adjustment factor, which adjusts for the extra loss in serviceability due to the number of unrepaired deteriorated joints, cracks, punchouts, and other discontinuities in the existing slab prior to the overlay; F_{dur} stands for durability adjustment factor, which adjusts for the extra loss in serviceability due to the presence and severity of durability problems in the existing slab prior to the overlay; and F_{fat} stands for fatigue damage adjustment factor, which adjusts for past fatigue damage, as indicated by the number of punchouts per mile that might exist in the existing slab prior to the overlay. Guidelines for the selection of these adjustment factors can be found in Reference 11.

In the latter method, the condition factor is determined based on the remaining life of the existing pavement, computed as the ratio of traffic-to-date to traffic-to-failure, subtracted from 100 percent, as shown in equation (7) below:

$$RL = 100\left(1 - \frac{n}{N}\right) \tag{7}$$

where:

$RL =$ remaining life, in percent

$n =$ traffic to date, in 18-kip ESAL

$D_e =$ traffic to failure, in 18-kip ESAL

Figure 2.4 is used to determine the value of the condition factor based on the estimated remaining life of the existing pavement.

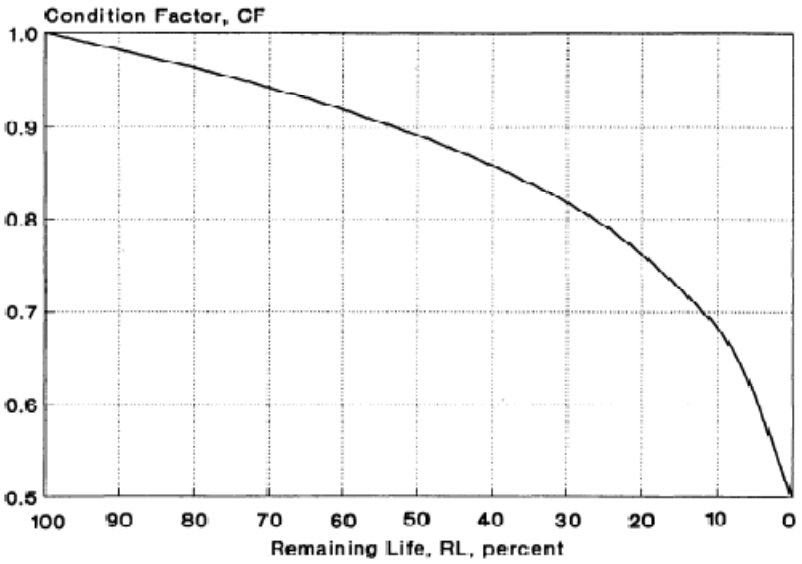

Figure 2.4: Relationship between condition factor and remaining life
(Source: AASHTO 1993, Figure 5.2.)

For this method, the slab thickness to carry future traffic, D_f, is calculated by means of the standard AASHTO rigid pavement design equation, as if it were a new pavement design.

2.4.4 MEPDG

The MEPDG and accompanying software represent the latest tool for the design and analysis of new and rehabilitated pavement structures. In this design methodology, a new philosophy is adopted: the application of mechanistic principles to carry out detailed distress development computations over the design life of the pavement structure. As a result, this design procedure provides the designer the opportunity to account for changes in loading and material properties, as well as direct consideration of the climatic effects on pavement performance.

For bonded overlaid CRCPs, it is assumed that the punchout failure mechanism for BCOs is not different than that of a new full-depth CRCP [12, 13]. Consequently, in developing this method, full depth punchouts were selected as the major structural distress type. In order to characterize the behavior of the BCOs, Zollinger's proposed failure mechanism was employed [12, 13]. According to Zollinger, punchout formation is closely related to the development of longitudinal fatigue cracks, located about 2 to 5 feet from the longitudinal edge of the slab, as a result of crack load transfer efficiency loss, severe base erosion and loss of support. Important milestones in the deterioration of the pavement structure leading to punchouts are indicated schematically as 1 though 5 in Figure 2.5.

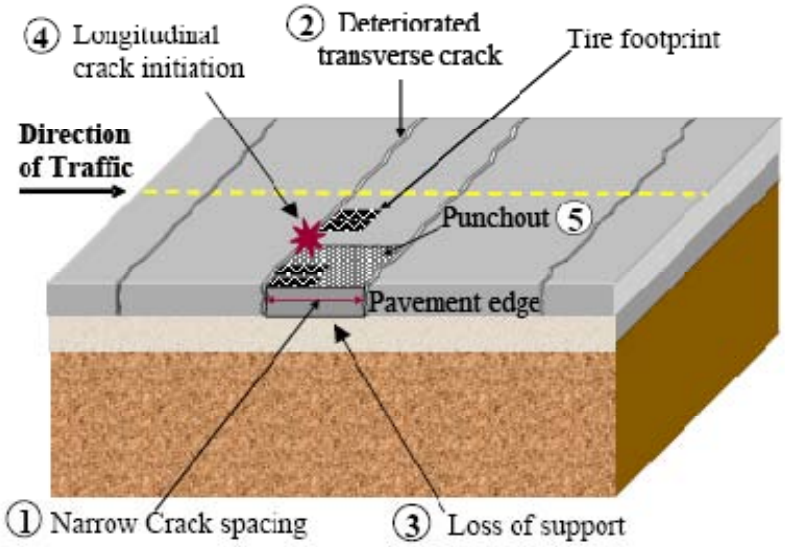

Figure 2.5: Mechanism of punchout development
(Source: NCHRP I-37, Appendix LL, 2003, Figure 2)

In order to predict performance, the design procedure requires both a study of the functional behavior as well as a study of the structural behavior of the pavement system. In the case of the study of the structural behavior of the pavement system, punchout prediction starts with the accumulation of fatigue damage over time as a function of the induced tensile stresses at the top surface of the overlay. Then, the accumulated fatigue damage is converted to number of punchouts using an empirical prediction model developed using data from the Long Term Pavement Performance (LTPP) program database [12, 13]. This failure mechanism, due to the assumptions made, is not applicable for CRCP with tied-concrete shoulder. In Texas, the use of tied-shoulder is a normal practice, and this mechanism needs revisions.

In the case of the functional behavior model, a linear regression model was developed to predict the international roughness index (IRI) score at the end of the design life of the pavement

structure. For CRCP, the IRI over the design period is function of the initial as-built roughness, the predicted number of punchouts and a site factor that takes into considerations other parameters of the pavement structure such as pavement age, location, and foundation characteristics.

2.5 Summary

The results of this literature review indicate that there is not a unified approach to bonded overlay design methods. All methods employ different failure criteria. The U.S. Army Corps of Engineers method was developed for plain concrete airport pavements and defines failure as the first appearance of structural cracking. In the case of AASHTO, the method is based on the observed behavior of jointed concrete pavements (JCP) and the failure criterion is based on the loss of serviceability. In the case of PCA, the method is based on the structural behavior of JCP and the failure criterion is based on stress limits established from the observed structural response of plain concrete specimens subject to fatigue testing. Moreover, none of these methods have been developed with due consideration of the principal failure mode observed in BCOs in CRCP: punchouts. Moreover, all these methods imply that there is no difference in the structural behavior of JCPs and CRCPs.

With respect to the MEPDG design method, it is clear that it represents a major step forward, as it is the first mechanistic-empirical design that takes into account punchout development. However, as described above, this method does not properly simulate punchout mechanisms in CRCP with tied-concrete shoulder. Also, it is important to note that, although all methods recognize the importance of attaining a perfect bond between the overlay and the substrate, they do not address this aspect directly.

Therefore, it is imperative that debonding be included as a distress mechanism for design of BCOs. To that end, the purpose of this study is to investigate debonding mechanisms under environmental loading at an early age and, based on an evaluation of these mechanisms, develop a mechanistic model capable of determining the extent of debonding for a variety of material, geometric and environmental conditions.

Chapter 3. Mechanistic Modeling of Debonding in BCO

3.1 Introduction

This chapter deals with the application of computational mechanics to predict the extent of debonding in BCOs subject to various environmental loading conditions at early ages. To that end, DIANA [18], a multipurpose, highly regarded finite element software that includes a wide range of material models for the analysis of non-linear behavior of concrete was used.

3.2 Debonding Behavior

In mathematical terms, strains in concrete induced by environmental loading and creep can be expressed as follows:

$$\varepsilon = \varepsilon_{sh} + \varepsilon_T + \varepsilon_e + \varepsilon_C \quad (8)$$

where:

ε = total strain

ε_{sh} = shrinkage strain

ε_T = thermal strain

ε_e = strain due to stress

ε_C = creep strain

In the above expression, tensile strains were considered to be positive, while compressive strains were considered to be negative. For computing stresses at early ages, it is conservative to neglect the creep effect.

In any type of structure subject to strain-induced loading such as shrinkage and thermal loading, stresses will not develop without some degree of restraint. In the case of BCOs, because the overlay is contracting from drying shrinkage (while the existing pavement is no longer subject to drying shrinkage) and because the bonded concrete overlay experiences greater temperature differentials than the existing pavement, differential volume changes exist, which in turn cause shear and tensile interface stresses to develop. When the tensile or shear stresses at the interface exceed the available bond strength, debonding may occur.

3.3 Development of the Debonding Model

As it has been previously noted, bonded concrete overlays are a rehabilitation procedure in which a layer of concrete is placed over the existing pavement to form a monolithic structure. As in the case of new CRCPs, BCOs are allowed to crack in a random pattern. Traditionally, cracking of the overlay is thought to be initiated at the bottom of the overlay, directly on top of the cracks in the existing pavements, extending upwards towards the surface (reflective cracks). However, investigations of both new and in-service overlaid pavements in Texas have shown that many non-reflective cracks develop [5, 6]. These types of cracks are believed to be initiated at the top of the overlay, as a result of thermal loading and shrinkage, progressing downwards towards the existing pavement (top-down cracks) [14].

In order to determine which type of cracking is more likely to occur in BCOs, a limited analytical study was conducted to identify the location of the critical tensile stress in the overlay

at an early age of the life of the pavement. To that end, a two dimensional finite element model of the pavement system, shown in Figure 3.1, was constructed using DIANA. For simplicity, the effect of steel reinforcement was not considered in the analysis.

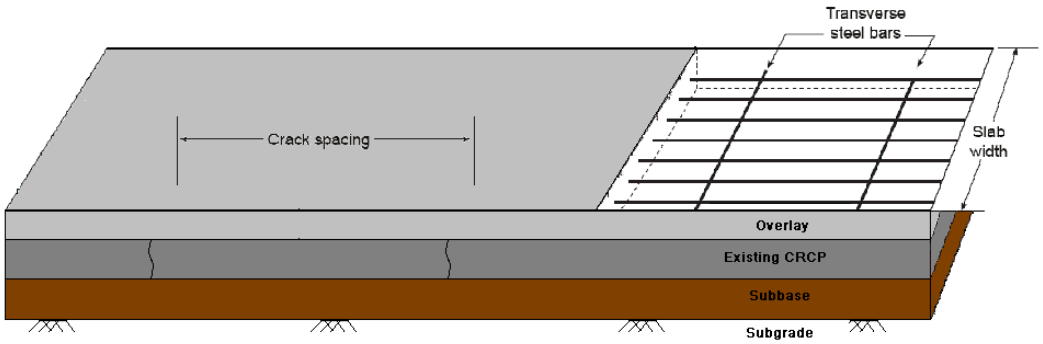

Figure 3.1: Cut-away section of a CRCP immediately after placement of the BCO

Variables considered in the study included overlay thickness and thermal loading gradient. For concrete layers, 8-noded quadrilateral plane-stress elements were used. To model the transverse crack in the existing pavement, structural interface elements that allow both normal and shear slips to occur between the two adjacent crack faces according to a brittle behavior were used. For all other constituents of the pavement system, including the interface between the overlay and the existing pavement and the foundation layers, structural interface elements were used. A schematic of the model is presented in Figure 3.2.

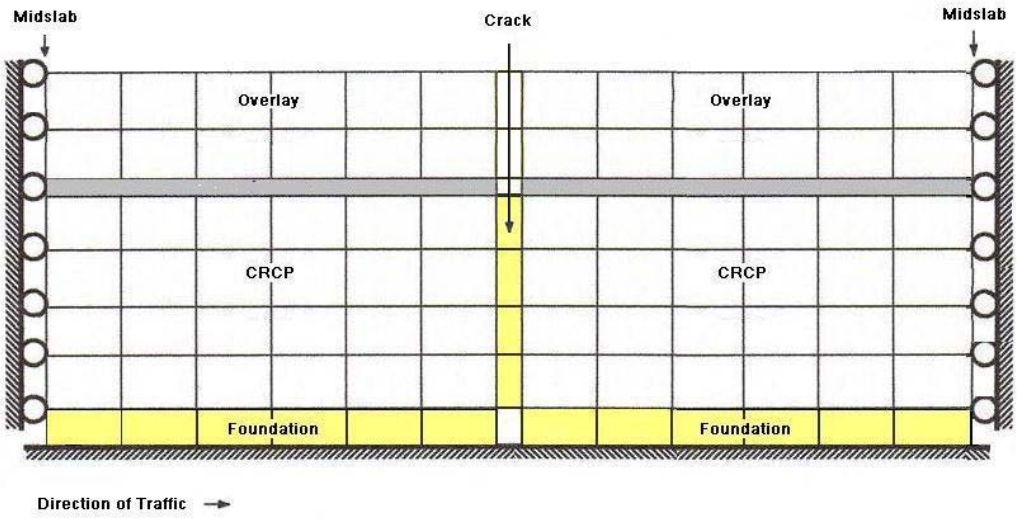

Figure 3.2: Schematic of the 2-dimensional model used for the critical stress location preliminary study

Figure 3.3 shows the results of the preliminary analysis. Plots of the deformed shape of the pavement system, depicting the location of the maximum longitudinal stress (σ_{XX}) in the overlay directly on top of the existing crack and near the surface of the overlay for all analysis runs together with a table detailing all analysis results are presented in Appendix A.

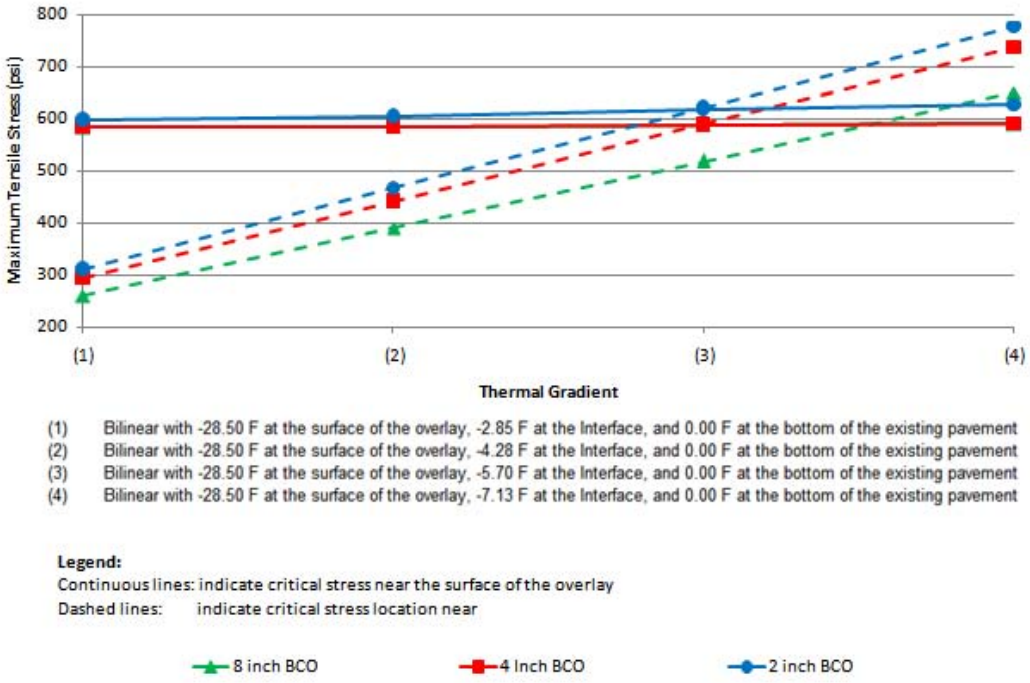

Figure 3.3: Plot of preliminary analysis results

As can be observed from Figure 3.3., both overlay thickness and thermal gradients play an important role in the determination of the location of the critical stress. With increasing overlay thicknesses, the effect of transverse cracks in the existing pavement is diminished. In the case of thermal gradients, loading conditions that place a highest portion of the thermal gradient at the overlay reduce the effect of transverse cracks in the existing pavement.

For non-reflective cracks, it is important to note that the horizontal distance between the transverse section, where the critical stress occurred, and the transverse section, where the crack in the existing pavement was located, varied as a function of the overlay's thickness. Consequently, no prescribed location for top-down cracking could be determined. However, the model did show that both non-reflective cracks and reflective cracks could indeed be caused by thermally induced stresses. From the point of view of modeling debonding behavior, this study failed to conclusively establish a uniform mechanism for transverse crack formation for BCOs. As a result, two pavements systems, as shown in Figure 3.4, were considered for modeling. These two models characterize debonding from the perspective of reflective cracks and non-reflective cracks (top-down), respectively. Note that in the non-reflective crack debonding model, the introduction of the vertical interface elements directly below the crack in the overlay responds to the need for analyzing whether or not the top-down crack in the overlay will puncture the existing CRCP slab.

a)

b)

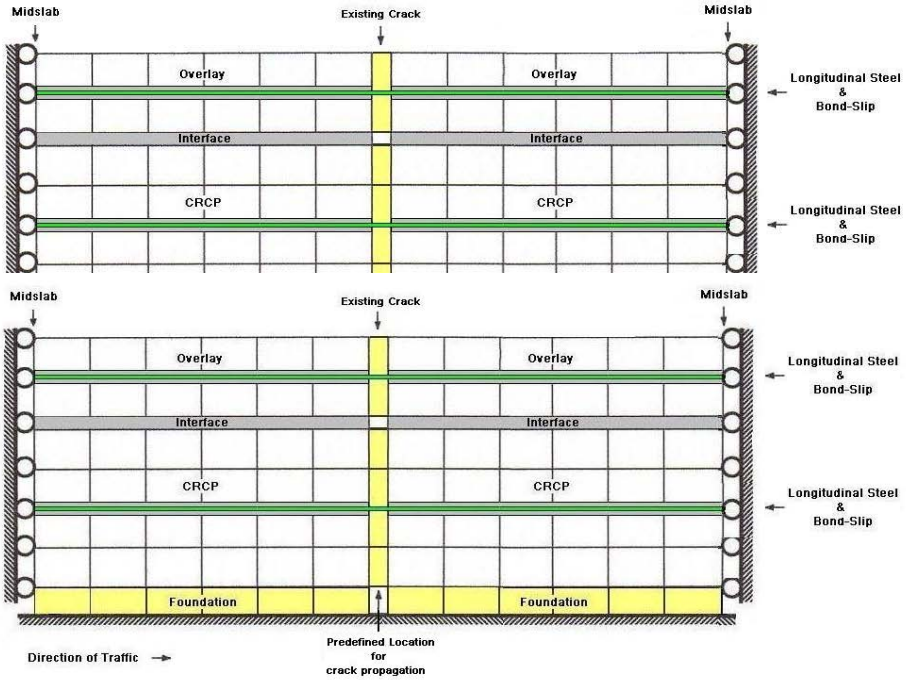

Figure 3.4: A) Reflective crack debonding model B) Non-reflective crack debonding model

For concrete layers, 8-noded quadrilateral plane-stress elements were used. Reinforcing steel was discretized using 2-noded truss elements. To model the effect of discontinuities, structural interface elements that allow both normal and shear slips to occur between the two adjacent crack faces were used. For all other constituents of the pavement system, including bond-slip between concrete and longitudinal steel, foundation layers, and the interface between the overlay and the existing pavement, structural interface elements were used. In the following sections, the behavior of each constitutive material, their interactions, and the chosen material models will be discussed. However, since a complete description of the underlying theory is beyond the scope of this research study, it will not be presented herein. If required, additional information on the application of non-linear elastic fracture mechanics to the modeling of the behavior of concrete and other cementitious materials can be found in [15, 16, 17, 18].

3.3.2 Concrete

Experimental and analytical studies carried out to investigate the failure mode of concrete specimens under uniaxial tensile loading have evidenced that, contrary to common believe, concrete is not completely brittle [17, 19, 20, 21]. Instead, it exhibits a moderate strain-hardening stage before it reaches its ultimate tensile capacity, followed by a stage characterized by the increase in deformation with decreasing tension carrying capacity, as depicted in Figure 3.5.

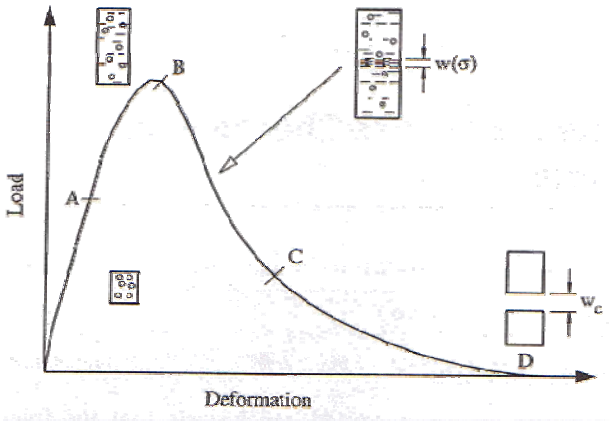

Figure 3.5: Typical tensile load-deformation response of a pre-cracked concrete specimen (Karihaloo B. L., 1995, Figure 1.1)

Based on micro-structural investigations of concrete specimens, the post-peak tension softening response of concrete is believed to be a consequence of the fact that concrete's microstructure is full of complexities. In particular, the interfacial transition zone between coarse aggregate and cement paste, and the existence of micro-cracks and voids, even before the structure is subject to external loading, are believed to be the primary reasons for this type of response.

Based on the observation of concrete failure modes in uniaxial tension, Chen states the following:

> *"The direction of crack propagation in uniaxial tension is transverse to the stress direction. The initiation and growth of every new crack will reduce the available load-carrying area, and this reduction causes an increase in the stresses at critical crack tips. The decreased frequency of cracks arrest means that the failure in tension is caused by a few bridging cracks rather than by numerous cracks, as it is for compressive states of stress."* (Source: Mehta, P. K., and Monteiro P. J. M., "*Concrete Microstructure, Properties and Materials",* Prentice Hall, 2001.)

As shown in Figure 3.5, the behavior of concrete in uniaxial tension is very complex, and limited work has been completed regarding the theory and application of fracture mechanics to concrete. However, a review of literature documenting the merits and demerits of the various available fracture models suitable for quasi-brittle materials like concrete provided insight into which constitutive model might be the most adequate for the analysis of BCOs [16, 22].

For concrete's material behavior characterization, available models generally follow either the smeared or the discrete approach. The main distinctive difference between them is that in the discrete approach, the discontinuity is individually characterized by the use of interface elements at pre-specified locations, while the smeared approach deals with the phenomena in a macro-structural manner.

For the smeared approach, available models include: (i) smeared cracking with decomposed strain, (ii) total strain based models and (iii) plasticity based models, among others.

For the discrete approach, available models include: (i) interface models with decomposed relative displacements; (ii) total relative displacements and (iii) plasticity based models, among others.

In the present study, the need to capture the micro-structural behavior of concrete in fracture lead us to adopt the discrete crack model with total relative displacements to describe concrete's post-peak response. In using this approach, the behavior of the bulk concrete is decoupled from the behavior of the discontinuity. As such, the model assumes a linear stress-strain relationship with slope E for the bulk material, relaying on the structural interface elements to characterize the observed post-peak tension softening response of concrete.

3.3.3 Discontinuities

As noted above, the discrete crack model with total relative displacements was selected to model discontinuities. In developing the formulation that describes the mechanical behavior of developing cracks, the following assumptions were made:

- At cracks the post-peak tension softening behavior of concrete is characterized.
- Cracks are capable of transmitting shear stress through aggregate interlock.

Based on the aforementioned assumptions, a discrete crack model for Mode I fracture was selected for use. Figure 3.6 shows the fundamental fracture modes.

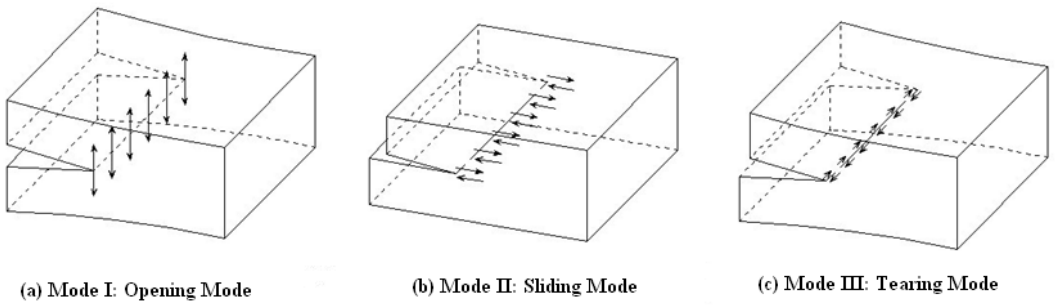

Figure 3.6: Fundamental fracture modes

Note that mode I corresponds to the normal separation of the crack under the effect of tensile stress applied normally to the crack plane. To describe the loss of stress transfer between two adjacent crack surfaces, a nonlinear relationship which expresses the tractions as a function of the total relative displacements (the crack width) was used. With regards to the shape of the strain-softening relation, linear, bilinear, polynomial and exponential approximations have been investigated with varying degrees of success. Based on numerical and experimental investigations of concrete specimens subject to both indirect and direct tension, Rots concluded the following:

> *"The exponential softening function proposed by Reinhardt et. al., with a tensile strength in the range between 2.5-3.5 N/mm2 (363-507 psi), and fracture energy in the range between 50-150 J/m2 (11-34 lbf*in/in2) serve as a fair set of parameters for standard concrete quantities."* (Source: Rots, J. G., "*Computational Modeling of Concrete Fracture",* Ph.D. Dissertation, Delft University, 1988, page 77).

In this study, an exponential softening function as proposed by Hordijk, Cornelissen, and Reinhardt [18] was used to characterize the post-cracking response (Figure 3.7).

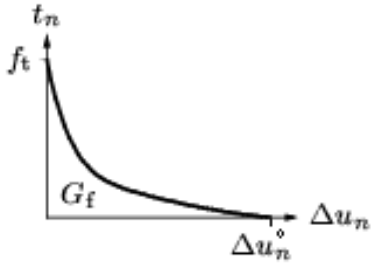

Figure 3.7: Mode I tension softening model – Hordijk et. al
(Source: DIANA 9,Material Library User Manual, 2005, Figure 9.10 – Modified).

In this case, the relationship of the crack stress is given by:

$$\frac{t_n}{f_t} = \left(1 + \left(c_1 \frac{\Delta u_n}{\Delta u_n^0}\right)^3\right) e^{\left(-c_2 \frac{\Delta u_n}{\Delta u_n^0}\right)} - \frac{\Delta u_n}{\Delta u_n^0}(1 + c_1^3) e^{-c_2} \quad (9)$$

where:
$c_1, c_2 = constants, 3\ and\ 6.93\ respectively$
$f_t = tensile\ strength$
$t_n = normal\ traction$
$\Delta u_n = normal\ relative\ displacement$
$\Delta u_n^0 = ultimate\ normal\ relative\ displacement = 5.136 \frac{G_f}{f_t}$
with:
$G_f = mode\ I\ fracture\ energy\ (area\ below\ the\ curve)$

With respect to the material parameters, values were derived as a function of concrete's compressive strength using the European CEB-FIP Model Code 1990 [18]. Table 3.1 shows suggested material parameters for the following concrete classes: C12, C20, C30, C40, C50, C60, C70, C80.

Table 3.1: Material Parameters suggested by CEB-FIP Model Code 1990

		Concrete Class							
		C12	C20	C30	C40	C50	C60	C70	C80
Characteristic Cyl. Comp Stress (Fck)	MPa	12	20	30	40	50	60	70	80
Mass Density	Kg/m^3	2500							
Poisson Ratio	:	0.1 <: <0.2							
Young Modulus (Eci)	MPa	27088	30303	33551	36268	38629	40733	42639	44388
Tensile Strength (Fctm)	MPa	1.581	2.222	2.912	3.528	4.094	4.623	5.123	5.600
Fracture Energy (Gf)	J/m^2	49	62	76	90	103	115	126	137
Shear Retention Factor	:	0.01							

		Concrete Class							
		C12	C20	C30	C40	C50	C60	C70	C80
Characteristic Cyl. Comp Stress (Fck)	psi	1740	2901	4351	5802	7252	8702	10153	11603
Mass Density	lb/in3	0.09							
Poisson Ratio	:	0.1 <: <0.2							
Young Modulus (Eci)	psi	3928825	4395133	4866094	5260169	5602673	5907752	6184209	6437939
Tensile Strength (Fctm)	psi	229	322	422	512	594	670	743	812
Fracture Energy (Gf)	$lbf*inch/inch^2$	11	14	17	20	23	26	28	31
Shear Retention Factor	:	0.01							

For this study, the existing pavement's compressive strength was estimated at 42.4 MPa (6,151 psi); based on reported test results from cores extracted from an in-service BCO candidate pavement section on IH-10 in El Paso, Texas [15]. Calculated material properties using the provisions included in CEB-FIP are presented in Table 3.2.

Table 3.2: Material Parameters for Developing Cracks

Tensile Strength (Fctm)	psi	532
Fracture Energy (Gf)	lbf*inch/inch^2	21
Shear Retention Factor	>	>

In addition, DIANA offers criteria for full and constant shear retention upon cracking. In this study, a constant shear retention factor $\beta = 0.01$ was introduced to impose a reduction of the shear stiffness upon cracking, as suggested by CEB-FIP. In addition, to simulate the undamaged condition prior to the violation of the crack initiation criterion, large normal and tangential interface stiffness values were prescribed.

In the case of existing cracks, the following assumptions were made:

- At cracks, all tension is carried by the steel reinforcement.
- Cracks are capable of transmitting shear stress through aggregate interlock.

Based on the aforementioned assumptions, a discrete crack model for Mode I fracture was selected for use. In this case, cracking is characterized by the full reduction of the strength after crack initiation, as depicted in Figure 3.8.

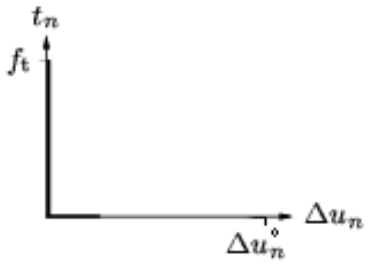

Figure 3.8: Mode I brittle cracking behavior
(Source: DIANA 9, Material Library, 2005, Figure 9.10 – Modified).

In mathematical terms, this behavior can be written as:

$$\frac{t_n}{f_t} = \begin{cases} 1 \text{ if } \Delta u_n \leq 0 \\ 0 \text{ if } 0 < \Delta u_n < \infty \end{cases} \quad (10)$$

where:
f_t = *tensile strength*
t_n = *normal traction*
Δu_n = *normal relative displacement*

The proposed model simulates the behavior of pre-existing cracks through the adoption of a nil tensile strength and a shear retention factor $\beta = 0.01$, to account for stress transfer due to aggregate interlock.

3.3.4 Interface between the Overlay and the Existing Pavement

In general, the interface between two parts of any structure is subject to biaxial stresses. As such, its behavior is typically characterized using a yield function that shows a close resemblance with the Mohr-Coulomb friction criterion (Figure 3.9). In the case of the interface between new and old concrete in BCOs, it has been postulated that debonding is always initiated in tension (Mode I) [24, 25, 26, 27, 28].

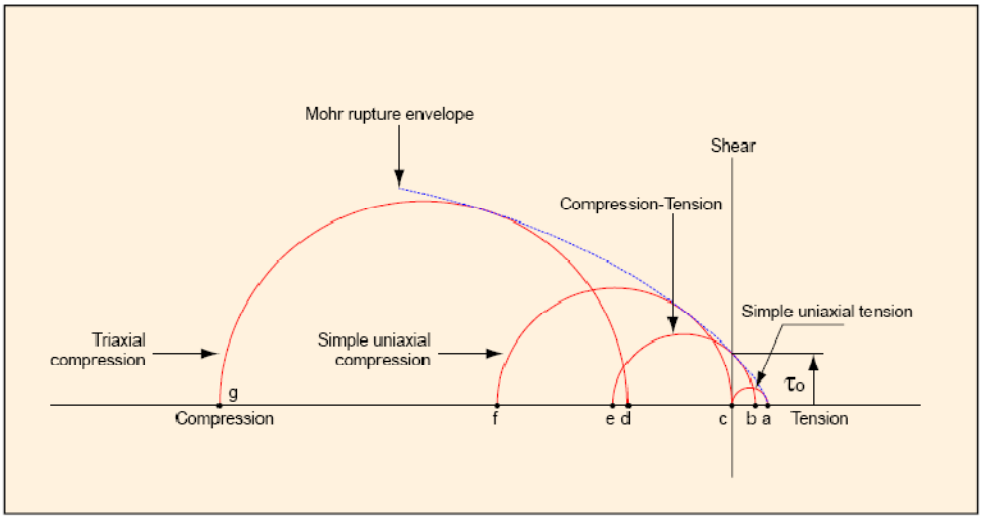

Figure 3.9: Typical Mohr-Coulomb rupture diagram for concrete (Source: Mehta, P. K., and Monteiro P. J. M., 2001, CD)

Consequently, as a first approximation, a Mohr-Coulomb constitutive model extended with a Mode I tension cut-off criterion was used to characterize the behavior of the interface. However, analysis results predicted by this model were in total disagreement with observed behavior, as they showed that as soon as debonding initiated, it propagated almost instantaneously along all the length of the interface. Based on an investigation of the causes that lead to this poor characterization of the debonding phenomenon, it became clear that the problem with such a model was that it failed to consider an important behavioral characteristic of debonding: the interlocking between the two faces of the debonding interface.

In order to account for tensile interlocking, a nonlinear relationship which expresses the normal tractions as a function of the debonding gap opening was used to describe the loss of stress transfer between the two faces of the debonding interface. The interlocking relationships governing the debonding interface behavior used in this study are presented in Figure 3.10. As a first approximation and in the lack of reliable data, an ultimate normal slip value of 0.05 mm (1.97 mils) was used for this study. Such value is in the same order of magnitude as values reported by Granju to have had been in good agreements with experimental results in his studies [25].

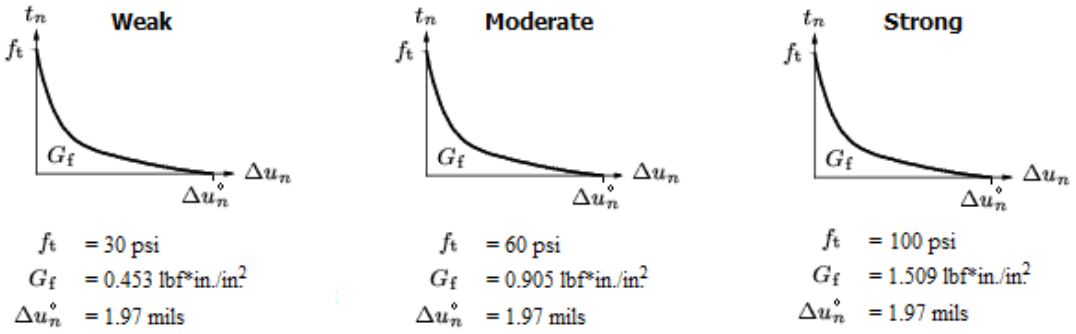

Figure 3.10: Mode I interlocking relationships for interface between new and old concrete.

In order to validate the adopted model, an analysis of the stress state at the location of debonding was made for every time step preceding debonding, for one analysis run. Figure 3.11 shows the results of this specific analysis. The red line represents the combined yield criterion of Mohr-Coulomb with tension cut-off. Material parameters describing the interface behavior were obtained from literature [14, 18, 25].

Tensile strength (*f*'t) = 0.414 MPa (60 psi).
Cohesion τ_0 = Estimated to be twice the tensile strength = 0.828 MPa (120 psi)
Friction angle (ϕ) = 30°

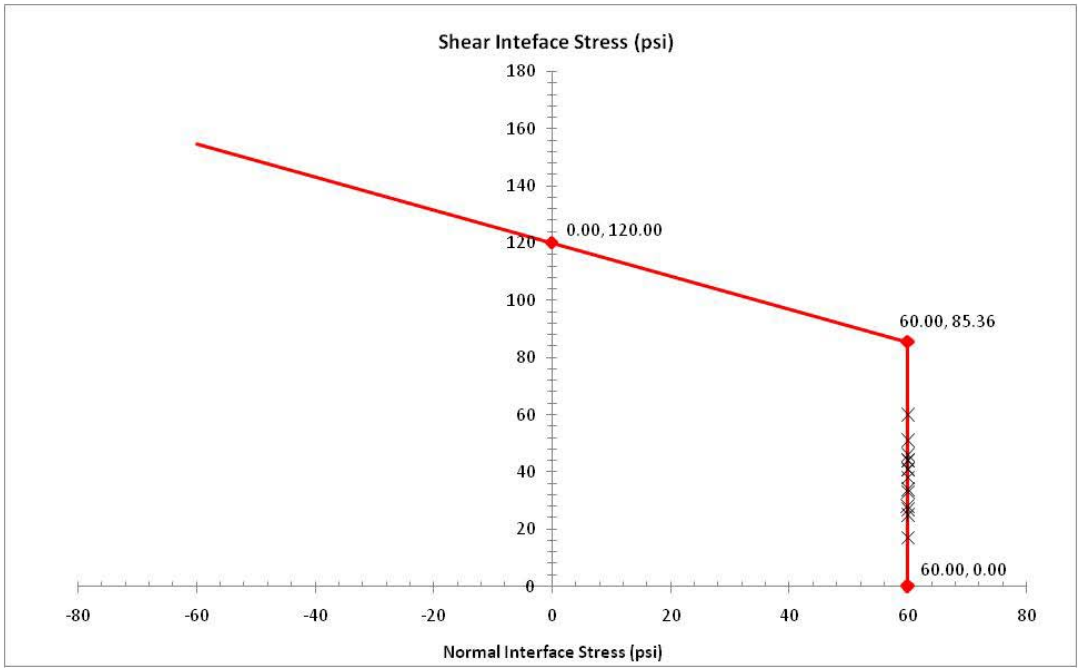

Figure 3.11: Observed debonding failure modes

From Figure 3.11, it can be observed that the induced tensile stresses perpendicular to the interface and the weaker tensile interface strength combined their effects so that the initiation and the propagation of debonding occurs in tension. Consequently, a model based on the assumption

that interface debonding initiates and propagates in tension normal to the interface (Mode I) seems to be valid.

3.3.5 Reinforcing Steel

In CRCP, the purpose of steel reinforcement is to hold cracked concrete together, therefore promoting load transfer through aggregate interlock and dowel action, preventing water percolation, and controlling transverse crack width and spacing.

In reinforced concrete pavements, like in any other reinforced concrete structure, reinforcing steel carries stresses primarily along the axis of the bar. Based on steel's stress-strain relationship under direct tension (Figure 3.12), its behavior can be divided into two stages. Initially, steel exhibits a linear elastic stage before it reaches its yield stress. This is followed by a plastic stage characterized first by the increase in strain demand at a constant stress, followed by a moderate strain-hardening response until it reaches its ultimate strength. Beyond this point, the specimen begins to neck and localized fracture occurs after the neck becomes unstable.

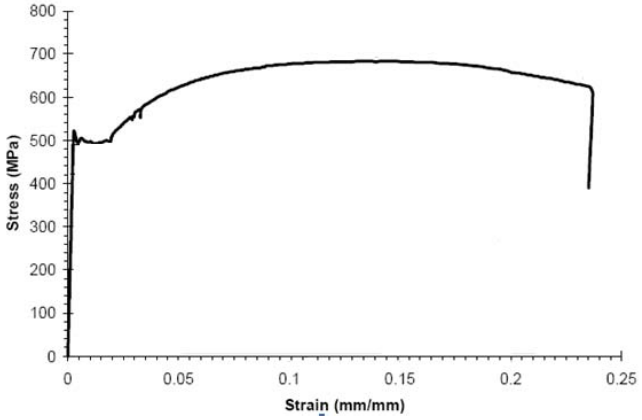

Figure 3.12: Typical uniaxial tensile stress-strain diagram for reinforcing steel bars (Lowes, L. N.,1999, Figure 3.2 - Modified)

For this study, the reinforcing steel was modeled as a linearly elastic material (Figure 3.13) as the reinforcing steel response in concrete pavements is typically well defined within the elastic range.

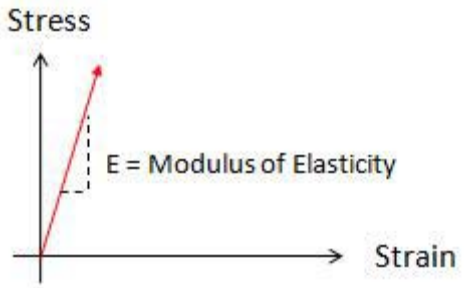

Figure 3.13: Reinforcing steel stress-strain relationship

Based on this model, the behavior of reinforcing steel is fully characterized by the ratio between the stress and the reversible strain, parameter commonly known as the modulus of

elasticity (E). In this study, a value of 200,000 MPa (29,000,000 psi) for both the overlay's reinforcement and the existing pavement's reinforcement was selected for use, which corresponds to the typical modulus of elasticity used for design.

3.3.6 Bond-Slip Relationship between Concrete and Longitudinal Steel

As described by Kwak et. al. [30], bond-slip is a stress transfer mechanism between reinforcing steel and concrete attributed to three different phenomena: (i) Chemical adhesion between mortar paste and steel bar surface; (ii) friction and wedging action of small dislodged sand particles between the bar and the surrounding concrete and; (iii) mechanical interaction between concrete and steel.

In this study, the aggregated interaction between concrete and reinforcing steel was characterized using interface elements with a multi-linear relation between the shear tractions and the shear relative displacements, as shown in Figure 3.14. Specific values selected for use were selected from a previous research study conducted by Dr. Moon Won at the Center for Transportation Research at The University of Texas at Austin [31].

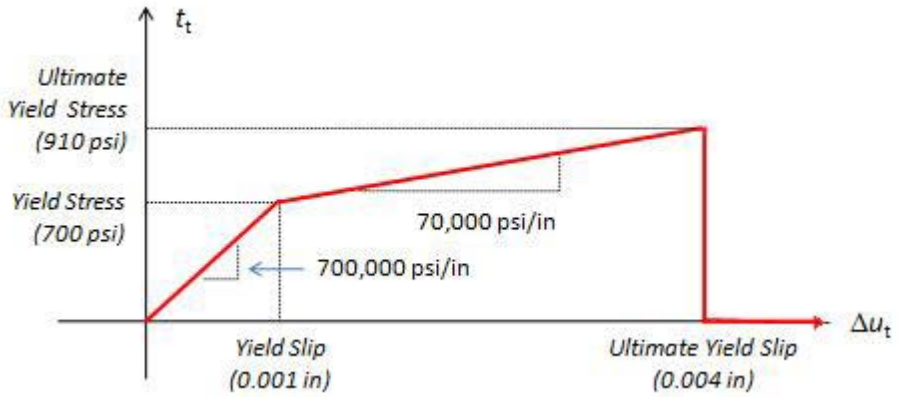

Figure 3.14: Bond-slip relationship

In the transverse direction, the relationship between normal traction and normal relative displacements was kept linear, but a large interface stiffness was prescribed in order to keep the normal deformation to a minimum.

3.3.7 Foundation Layers

Rigid pavements are generally placed either on a single layer of granular or stabilized material over a prepared subgrade, or directly over the prepared subgrade. Thus, the typical cross section of a rigid pavement structure consists of a PCC slab, a base or subbase course, a compacted subgrade, a natural subgrade and the bedrock, as shown in Figure 3.15.

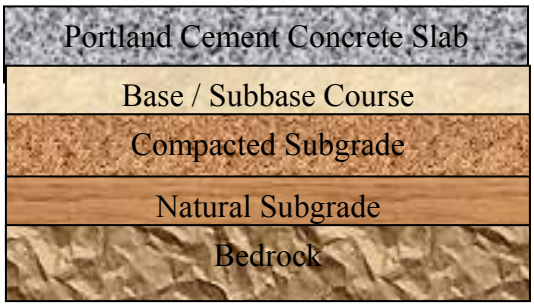

Figure 3.15: Typical material composition of a rigid pavement structure

Although all layers can be modeled using finite elements, for computational convenience, complete modeling of the underlying layers was not considered. Instead, the aggregated structural response of the foundation layers was characterized using interface elements with a linear relation between normal tractions and normal relative displacements in compression and zero stiffness in tension, as shown in Figure 3.16.

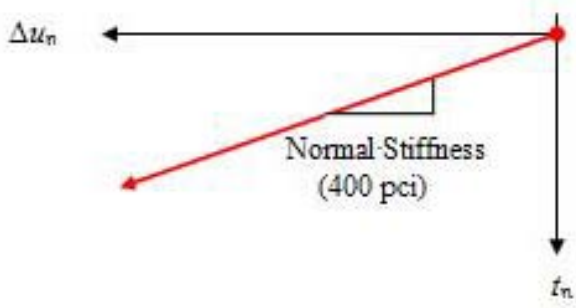

Figure 3.16: Effective stiffness of the foundation layers

In the tangential direction, the relationship between shear tractions and shear relative displacements was initially kept linear, up to a yield slip of 0.02 inches, followed by a stage characterized by the increase in the shear relative displacements at a constant stress, as shown in Figure 3.17.

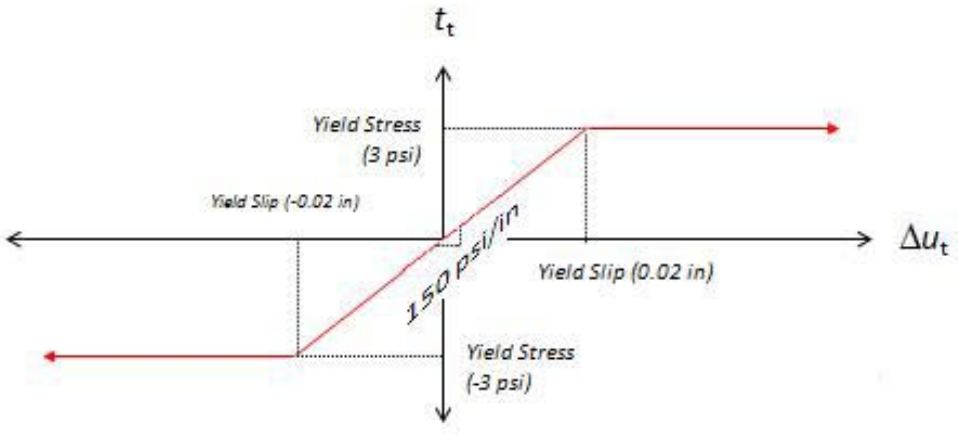

Figure 3.17: Slab-base/subbase bond-slip relationship

In both cases, the values used to characterize the behavior of the foundation layers were based on values reported in an earlier research study by Won [31].

Chapter 4. Sensitivity Analysis of Debonding Model

4.1 Introduction

Parametric studies were performed to evaluate the effects of design, material, and environmental conditions on the extent of debonding. To that end, knowledge gained from both computational modeling and field experience was used to identify the most important factors having an influence on debonding. These important factors are listed in Table 4.1.

Table 4.1: Factors having an Influence on Debonding

General	Time of Analysis
	Pavement System under Consideration
PCC Properties	Modulus of Elasticity
	Coefficient of Thermal Expansion
	Drying Shrinkage
	Creep
	Interface Strength
	Set Temperature
Steel Properties	Percent Reinforcement
	Bar Diameter
	Location of Steel Reinforcement
Environmental Conditions	Average Ambient Air Temperature
	Daily Ambient Air Temperature Variations
	Solar Radiation
	Wind Speed
	Relative Humidity
Dimension and Geometry of Pavement System	Original pavement thickness
	Overlay Thickness
	Transverse Crack Spacing
	Crack Widths

A comprehensive parametric study of all these factors, with each at only two levels, would require over 1,000,000 computer runs; a very time-consuming and expensive task. In order to reduce the analysis to a manageable size, some of the factors were eliminated, held constant, or combined, resulting in a more compact factorial experiment, as shown in Table 4.2. It should be noted that the effect of moisture gradients within the pavement structure were incorporated as equivalent thermal gradients. This reduced experiment resulted in 144 runs.

Table 4.2: Analysis Factorial

FACTOR	LEVELS	UNIT	VALUE		
			Low	Medium	High
Overlay Thickness	3	inch	4	6	8
Normal Interface Strength	3	psi	30	60	100
Thermal Coefficient of Overlay	2	in./in F	4.00E-06	--	6.00E-06
Thermal Coefficient of Existing Pavement	2	in./in F	4.00E-06	--	6.00E-06
Modulus of Overlay	2	psi	4.00E+06	--	5.00E+06
Existing Pavement Thickness	2	inch	8	--	10
Modulus of Existing Pavement	1	psi	--	4.00E+06	--

Before proceeding with the analysis, a set of trial runs were conducted to assess the ability of the models in predicting the initiation and the extent of debonding. Estimated debonding lengths for both the reflective crack debonding model and the non-reflective crack debonding model are presented in Table 4.3. The model's reference formulation for analysis consisted of a 4 inch overlay with a modulus of concrete of 5 x 10^6 psi over an 8 inch thick existing CRCP slab with a modulus of elasticity value of 4 x 10^6 psi and a coefficient of thermal expansion of 8 in./in °F. An ultimate normal slip value of 4.04 mils was used to characterize the loss of load transfer between the two faces of the debonding interface.

Table 4.3: Debonding Length for Various Interface Conditions

MODEL	BCO COEFFICIENT OF THERMAL EXPANSION	BOND INTERFACE STRENGTH		
		WEAK (30 psi)	MODERATE (60 psi)	STRONG (100 psi)
Non-Reflective Crack Debonding Model	4 in/in F	7.04 in.	3.37 in.	1.84 in.
Non-Reflective Crack Debonding Model	8 in/in F	17.76 in.	9.18 in.	4.59 in.
Reflective Crack Debonding Model	4 in/in F	0.00 in.	0.00 in.	0.00 in.
Reflective Crack Debonding Model	8 in/in F	3.06 in.	0.00 in.	0.00 in.

Contour plots of the principal stress (σ_1) and deformed shapes are presented in Figure 4.1 and Figure 4.2. Note that the color modulation ranges from red for the extreme positive value, through yellow and green, to blue, for zero stress.

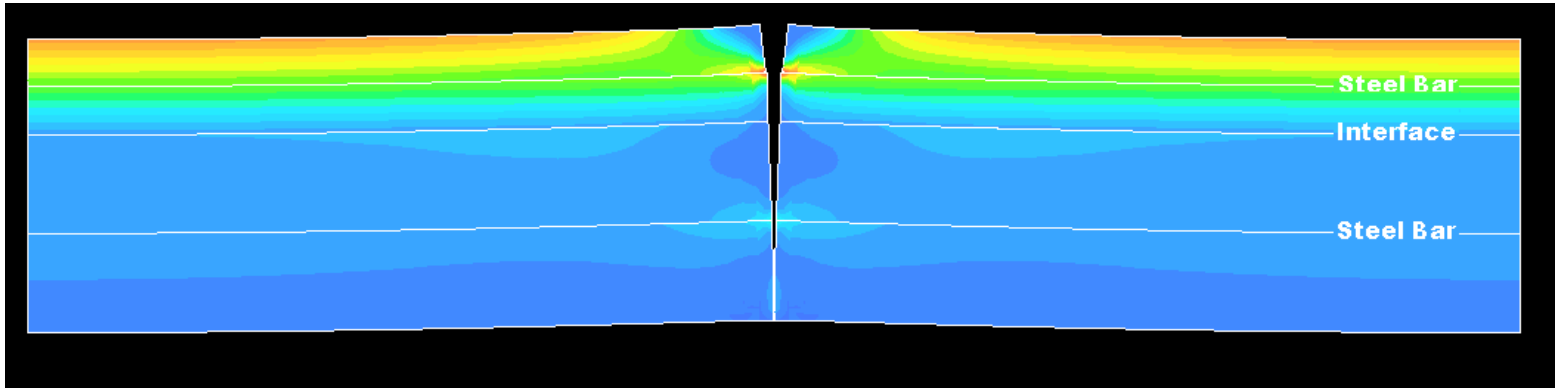

Figure 4.1: Deformed shape & contour plot of principal stress (σ_1)- Reflective crack debonding model

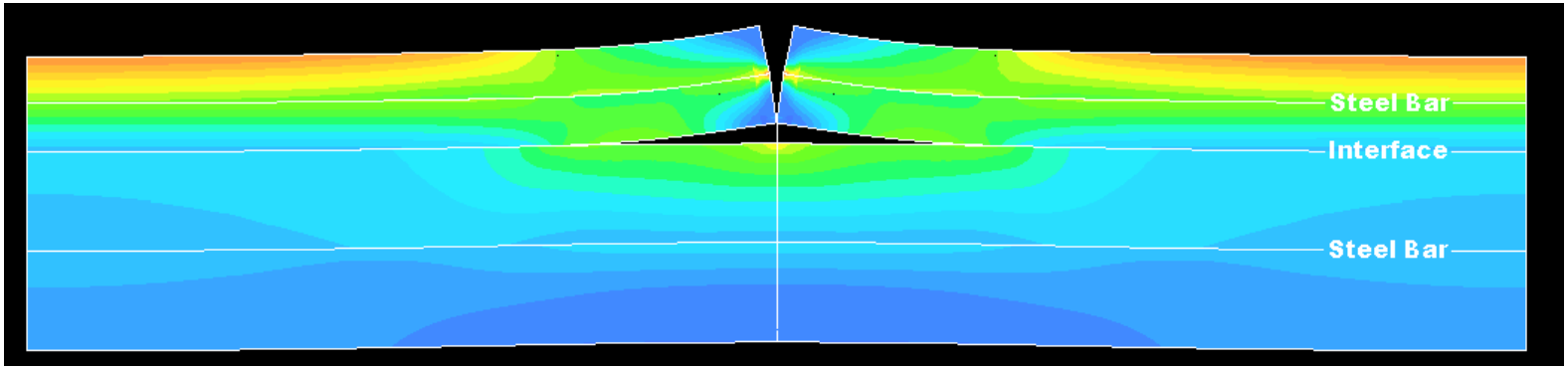

Figure 4.2: Deformed shape & contour plot of principal stress (σ_1)- Non-reflective crack debonding model -

An examination of the results shows that, from the point of view of debonding, the non-reflective debonding model is significantly more severe than the reflective crack debonding model. Therefore, a complete investigation of the behavior of the overlay using the combination of geometric and materials shown in Table 4.2. was only performed for the non-reflective crack debonding model (Figure 3.4 (B)).

In addition, it is important to note that, for the reflective crack debonding model, the behavior of the composite pavement closely resembles that of a new pavement structure. Moreover, an analysis of the stress state for the reflective crack model seems to indicate that, for negative thermal differentials, horizontal cracking will presumably occur at the interface between the overlay's reinforcement and the surrounding concrete, instead of at the interface between the new and old concrete.

An investigation of the early age behavioral characteristics of the BCO implicitly requires the consideration of the effects of time. Ideally, the problem should be analyzed with a time incremental approach which would allow for the incorporation of changing material and environmental conditions in a continuous manner. However, due to the practical limitations such an analysis would impose, this study only attempts to characterize the behavior of BCOs for one critical point in time.

As it has been previously stated, experience has demonstrated that debonding problems typically occur in the early ages of the BCO, as a result of large temperature and moisture properties. For this study, a temperature differential of -28°F was selected, as depicted in Figure 4.3. In order to obtain modulus data for the selected critical time of analysis (72 hours after placement), a hyperbolic growth function as that shown in Figure 4.4 was employed.

In the following sections, the results of the sensitivity analysis are discussed. A key to understanding the box and whisker plots in Figure 4.8 through Figure 4.20 is shown in Figure 4.5. Note that data points that are greater than 1.5 times the size of the box are denoted by an asterisk.

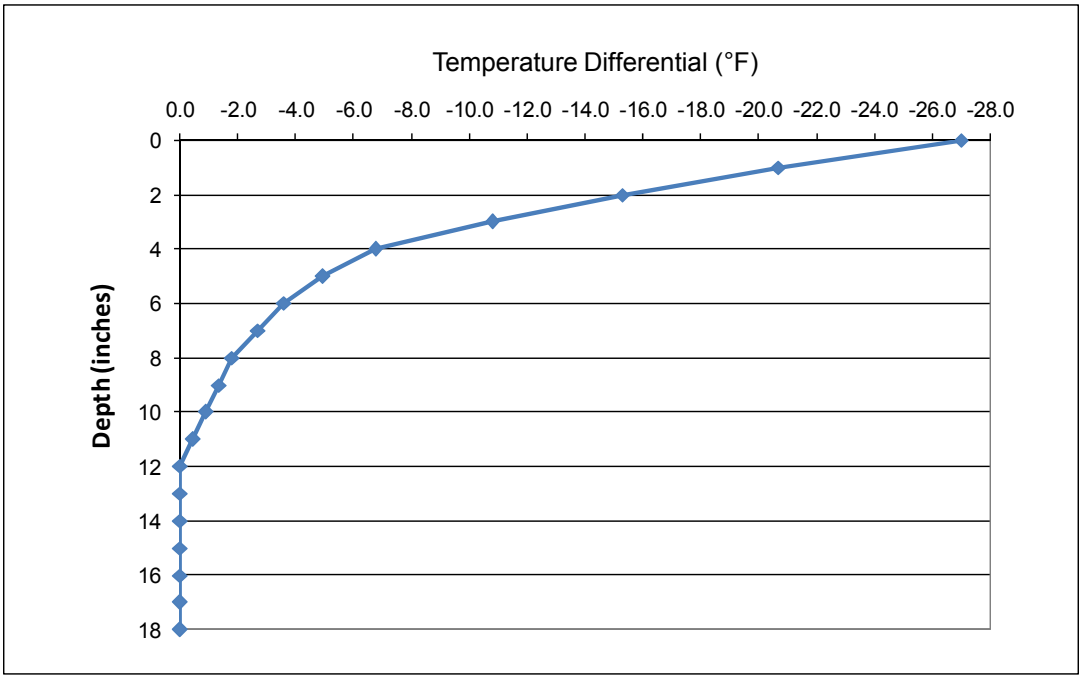

Figure 4.3: Thermal differential

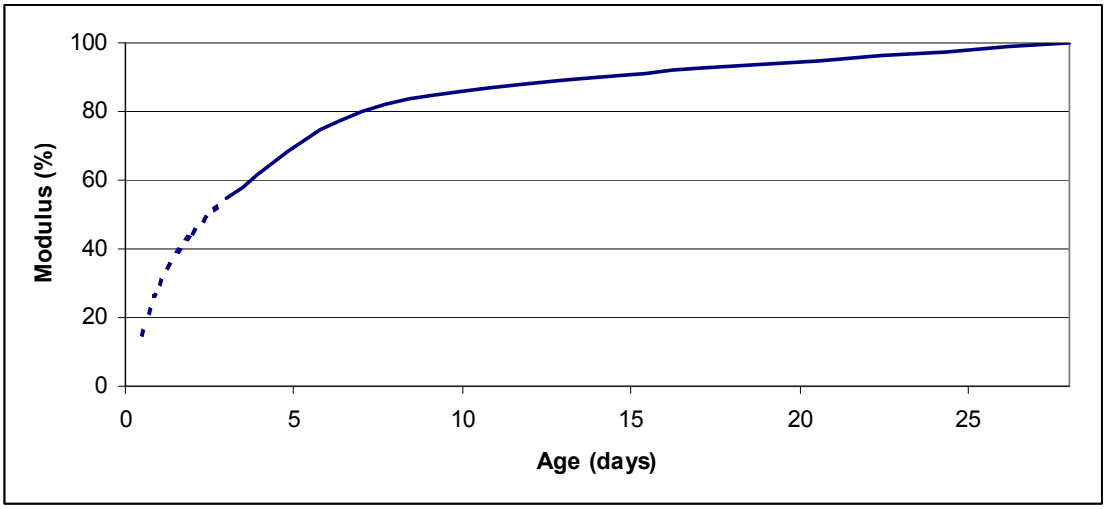

Figure 4.4: Schematic of the relationship between concrete age and 28-day modulus

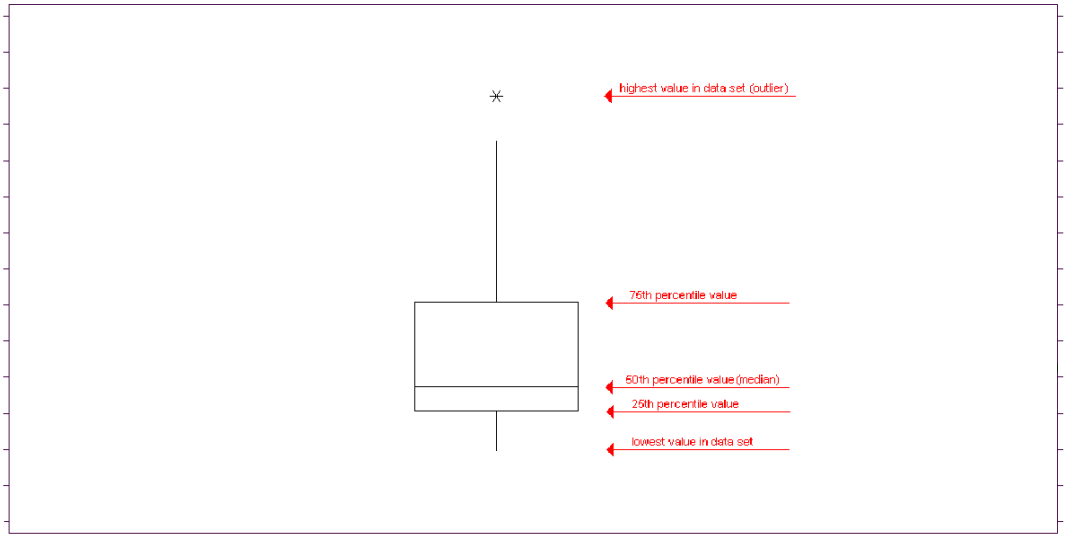

Figure 4.5: Key to understanding the box and whisker plots

4.2 Analysis Results

Results of the parametric study are presented in Table 4.4. Qualitatively similar results were obtained for all analysis runs. Therefore, for the sake of simplicity, only a complete description of the results for analysis run number 1 are presented here. Figure 4.6 shows the interface stresses (tractions) immediately before debonding initiation. Note that the maximum interface stress occurs at the vicinity of the non-reflective crack, with the stresses decreasing rapidly as we move away from the discontinuity. In the nonlinear analysis, 96 monotonic load steps of 0.2917 °F were executed. Since we used temperature differential increments in the nonlinear analysis, DIANA was used to create an animation of the behavior of the pavement system using several load steps. Figure 4.7 shows a 24 frame animation sequence of the deformation and the horizontal concrete stress. Note that all frames use the same color

modulation to set up the stress contours. From the animation sequence, the gradual progression of debonding can be observed. Note that debonding initiates at the tip of the crack in the overlay, after the transverse crack has traversed the entire depth of the overlay, and propagates in the longitudinal direction as a result of the overlay's curling action.

Table 4.4: Parametric Study Case Matrix with Results

CRCP Thickness	Overlay Thickness	Overlay Modulus	Overlay COTE	CRCP COTE	Interface Normal Strength	Case Number	Step at which Debonding Initiated (out of 96)	Debonding Length
8 inch	4 inch	4E+06 psi	4E-06 in/in*F	4E-06 in/in*F	30 psi	1	8	6.73 in.
					60 psi	2	15	3.06 in.
					100 psi	3	24	0.92 in.
				6E-06 in/in*F	30 psi	4	8	6.73 in.
					60 psi	5	15	3.06 in.
					100 psi	6	24	0.92 in.
			6E-06 in/in*F	4E-06 in/in*F	30 psi	7	5	13.16 in.
					60 psi	8	10	5.82 in.
					100 psi	9	16	3.06 in.
				6E-06 in/in*F	30 psi	10	5	13.16 in.
					60 psi	11	10	5.82 in.
					100 psi	12	16	3.06 in.
		5E+06 psi	4E-06 in/in*F	4E-06 in/in*F	30 psi	13	6	9.18 in.
					60 psi	14	11	4.29 in.
					100 psi	15	19	1.84 in.
				6E-06 in/in*F	30 psi	16	6	9.18 in.
					60 psi	17	11	4.29 in.
					100 psi	18	19	1.84 in.
			6E-06 in/in*F	4E-06 in/in*F	30 psi	19	4	18.98 in.
					60 psi	20	8	8.27 in.
					100 psi	21	13	4.29 in.
				6E-06 in/in*F	30 psi	22	4	18.98 in.
					60 psi	23	8	8.27 in.
					100 psi	24	13	4.29 in.
	6 inch	4E+06 psi	4E-06 in/in*F	4E-06 in/in*F	30 psi	25	8	9.18 in.
					60 psi	26	16	3.06 in.
					100 psi	27	26	1.53 in.
				6E-06 in/in*F	30 psi	28	8	9.18 in.
					60 psi	29	16	3.06 in.
					100 psi	30	26	1.53 in.
			6E-06 in/in*F	4E-06 in/in*F	30 psi	31	6	17.45 in.
					60 psi	32	11	7.96 in.
					100 psi	33	18	3.06 in.
				6E-06 in/in*F	30 psi	34	6	17.45 in.
					60 psi	35	11	7.96 in.
					100 psi	36	18	3.06 in.
		5E+06 psi	4E-06 in/in*F	4E-06 in/in*F	30 psi	37	6	11.63 in.
					60 psi	38	12	4.59 in.
					100 psi	39	20	1.84 in.
				6E-06 in/in*F	30 psi	40	6	11.63 in.
					60 psi	41	12	4.59 in.
					100 psi	42	20	1.84 in.
			6E-06 in/in*F	4E-06 in/in*F	30 psi	43	4	22.96 in.
					60 psi	44	8	10.41 in.
					100 psi	45	14	4.59 in.
				6E-06 in/in*F	30 psi	46	4	22.96 in.
					60 psi	47	8	10.41 in.
					100 psi	48	14	4.59 in.
	8 inch	4E+06 psi	4E-06 in/in*F	4E-06 in/in*F	30 psi	49	9	9.18 in.
					60 psi	50	18	3.06 in.
					100 psi	51	29	0.92 in.
				6E-06 in/in*F	30 psi	52	9	9.18 in.
					60 psi	53	18	3.06 in.
					100 psi	54	29	0.92 in.
			6E-06 in/in*F	4E-06 in/in*F	30 psi	55	6	18.06 in.
					60 psi	56	12	7.96 in.
					100 psi	57	20	3.06 in.
				6E-06 in/in*F	30 psi	58	6	18.06 in.
					60 psi	59	12	7.96 in.
					100 psi	60	20	3.06 in.
		5E+06 psi	4E-06 in/in*F	4E-06 in/in*F	30 psi	61	7	11.94 in.
					60 psi	62	14	4.29 in.
					100 psi	63	23	1.84 in.
				6E-06 in/in*F	30 psi	64	7	11.94 in.
					60 psi	65	14	4.29 in.
					100 psi	66	23	1.84 in.
			6E-06 in/in*F	4E-06 in/in*F	30 psi	67	5	22.96 in.
					60 psi	68	9	10.41 in.
					100 psi	69	15	4.29 in.
				6E-06 in/in*F	30 psi	70	5	22.96 in.
					60 psi	71	9	10.41 in.
					100 psi	72	15	4.29 in.

Table 4.4: Parametric Study Case Matrix with Results (Cont.)

CRCP Thickness	Overlay Thickness	Overlay Modulus	Overlay COTE	CRCP COTE	Interface Normal Strength	Case Number	Step at which Debonding Initiated (out of 96)	Debonding Length
10 inch	4 inch	4E+06 psi	4E-06 in/in*F	4E-06 in/in*F	30 psi	73	8	7.04 in.
					60 psi	74	15	3.06 in.
					100 psi	75	25	0.92 in.
				6E-06 in/in*F	30 psi	76	8	7.04 in.
					60 psi	77	15	3.06 in.
					100 psi	78	25	0.92 in.
			6E-06 in/in*F	4E-06 in/in*F	30 psi	79	5	14.39 in.
					60 psi	80	10	6.43 in.
					100 psi	81	17	3.06 in.
				6E-06 in/in*F	30 psi	82	5	14.39 in.
					60 psi	83	10	6.43 in.
					100 psi	84	17	3.06 in.
		5E+06 psi	4E-06 in/in*F	4E-06 in/in*F	30 psi	85	6	9.49 in.
					60 psi	86	12	4.29 in.
					100 psi	87	19	1.84 in.
				6E-06 in/in*F	30 psi	88	6	9.49 in.
					60 psi	89	12	4.29 in.
					100 psi	90	19	1.84 in.
			6E-06 in/in*F	4E-06 in/in*F	30 psi	91	4	21.43 in.
					60 psi	92	8	9.18 in.
					100 psi	93	13	4.29 in.
				6E-06 in/in*F	30 psi	94	4	21.43 in.
					60 psi	95	8	9.18 in.
					100 psi	96	13	4.29 in.
	6 inch	4E+06 psi	4E-06 in/in*F	4E-06 in/in*F	30 psi	97	9	9.18 in.
					60 psi	98	17	3.06 in.
					100 psi	99	27	0.92 in.
				6E-06 in/in*F	30 psi	100	9	9.18 in.
					60 psi	101	17	3.06 in.
					100 psi	102	27	0.92 in.
			6E-06 in/in*F	4E-06 in/in*F	30 psi	103	6	17.76 in.
					60 psi	104	11	7.96 in.
					100 psi	105	18	3.06 in.
				6E-06 in/in*F	30 psi	106	6	17.76 in.
					60 psi	107	11	7.96 in.
					100 psi	108	18	3.06 in.
		5E+06 psi	4E-06 in/in*F	4E-06 in/in*F	30 psi	109	7	11.94 in.
					60 psi	110	13	4.59 in.
					100 psi	111	21	1.84 in.
				6E-06 in/in*F	30 psi	112	7	11.94 in.
					60 psi	113	13	4.59 in.
					100 psi	114	21	1.84 in.
			6E-06 in/in*F	4E-06 in/in*F	30 psi	115	5	24.18 in.
					60 psi	116	9	10.71 in.
					100 psi	117	14	4.59 in.
				6E-06 in/in*F	30 psi	118	5	24.18 in.
					60 psi	119	9	10.71 in.
					100 psi	120	14	4.59 in.
	8 inch	4E+06 psi	4E-06 in/in*F	4E-06 in/in*F	30 psi	121	9	10.41 in.
					60 psi	122	18	3.06 in.
					100 psi	123	30	0.92 in.
				6E-06 in/in*F	30 psi	124	9	10.41 in.
					60 psi	125	18	3.06 in.
					100 psi	126	30	0.92 in.
			6E-06 in/in*F	4E-06 in/in*F	30 psi	127	6	20.51 in.
					60 psi	128	12	9.18 in.
					100 psi	129	20	3.06 in.
				6E-06 in/in*F	30 psi	130	6	20.51 in.
					60 psi	131	12	9.18 in.
					100 psi	132	20	3.06 in.
		5E+06 psi	4E-06 in/in*F	4E-06 in/in*F	30 psi	133	7	14.08 in.
					60 psi	134	14	5.20 in.
					100 psi	135	23	1.84 in.
				6E-06 in/in*F	30 psi	136	7	14.08 in.
					60 psi	137	14	5.20 in.
					100 psi	138	23	1.84 in.
			6E-06 in/in*F	4E-06 in/in*F	30 psi	139	5	26.63 in.
					60 psi	140	9	12.55 in.
					100 psi	141	15	5.20 in.
				6E-06 in/in*F	30 psi	142	5	26.63 in.
					60 psi	143	9	12.55 in.
					100 psi	144	15	5.20 in.

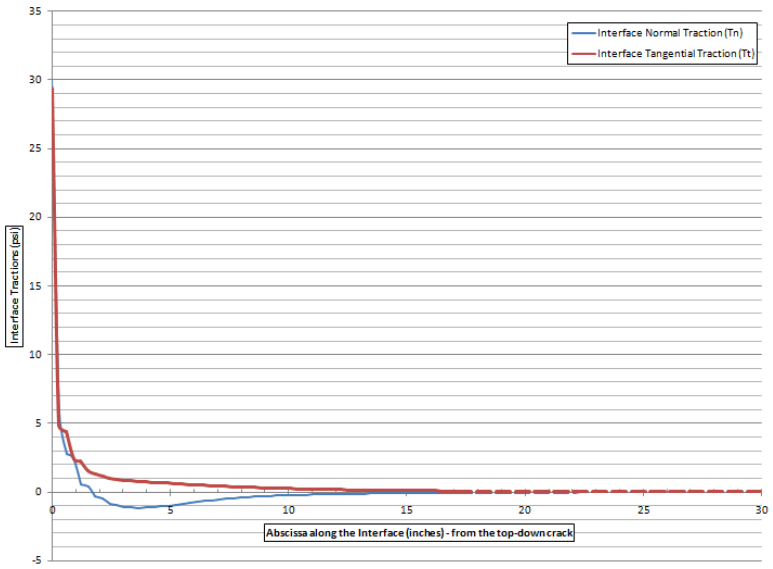

Figure 4.6: Interface stress immediately before debonding initiation

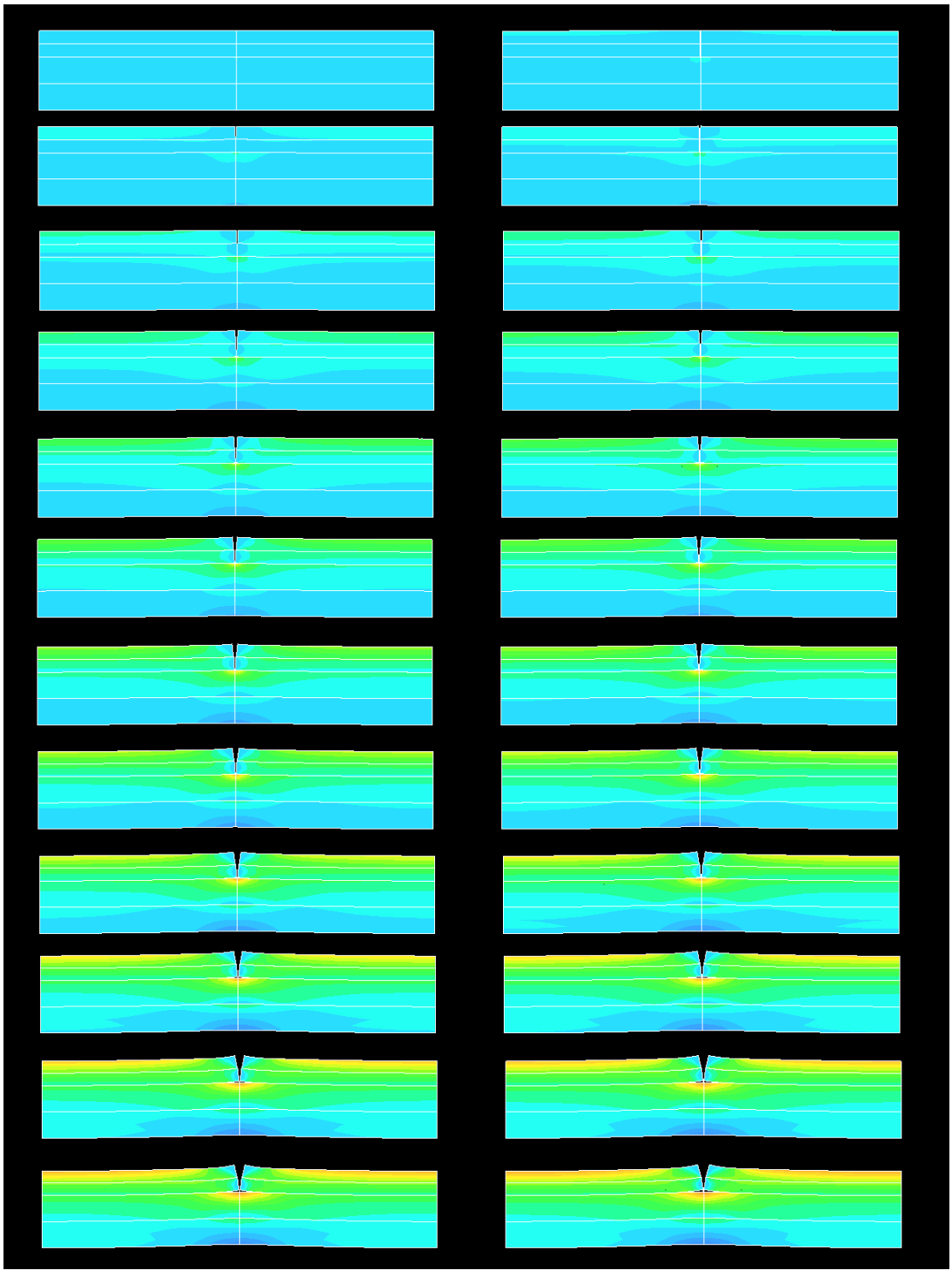

Figure 4.7: Animation of deformation and horizontal Stress

4.2.2 Effect of Bond Strength

Figure 4.8 indicates the relationship between debonding length and the tensile interface strength. As expected, the extent of debonding largely depends on the tensile interface strength value used for analysis. Note that only 25% of the structures with tensile interface strengths of 100 psi have more than 4 inches of debonding, whereas 75% of the structures with tensile interface strengths of 30 psi have more than 9 inches of debonding.

In addition to significantly reducing the amount of debonding, increasing bond strengths also delayed debonding initiation, as shown in Figure 4.9. For tensile interface strengths in excess of 300 psi, debonding may even be prevented, as suggested by an additional simulation run performed using the same formulation as for case number 3, shown in Table 4.4.

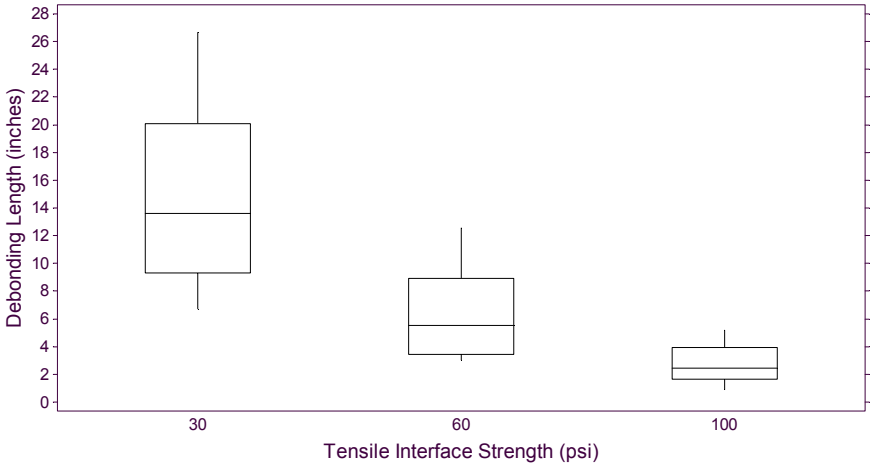

Figure 4.8: Effect of the tensile interface strength on the predicted amount of debonding length

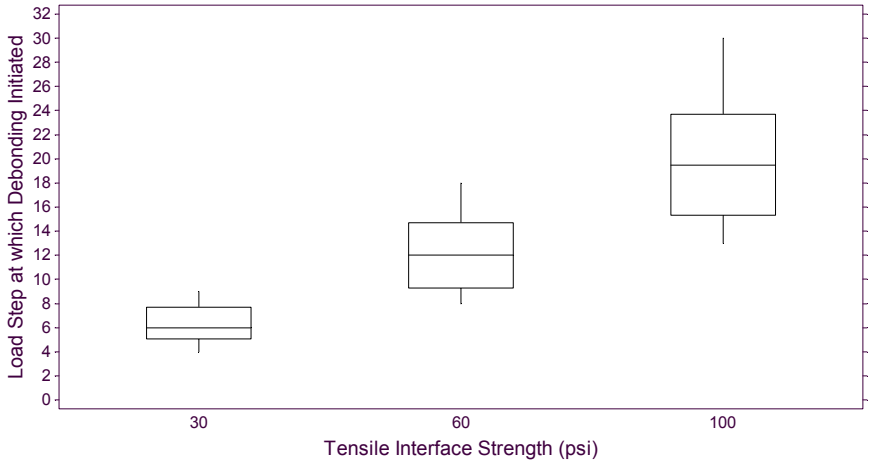

Figure 4.9: Effect of the of the tensile interface strength on debonding initiation

4.2.3 Effect of the Coefficient of Thermal Expansion of the Overlay

Results of the sensitivity analysis show that the coefficient of thermal expansion (CTE) of the overlay is a key parameter in controlling and mitigating the effects of severe environmental loads on BCOs. Figure 4.10 shows the variations in debonding length with

increases in the coefficient of thermal expansion of the overlay. The plot indicates that only 25% of the overlays with a CTE of 4 in./in. F exceeded a debonding length of 9 inches, whereas 50% of the overlays with a CTE of 6 in./in. F exceeded a debonding length of 9 inches.

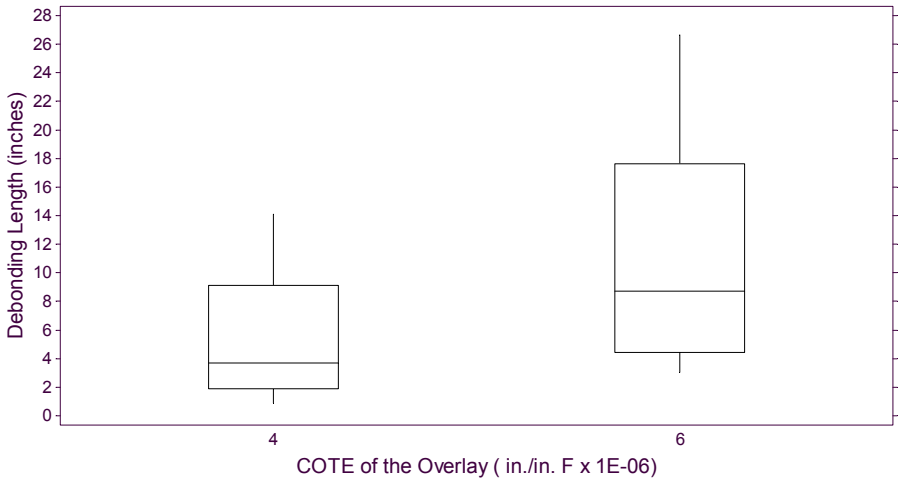

Figure 4.10: Effect of the overlay's CTE on the predicted amount of debonding length

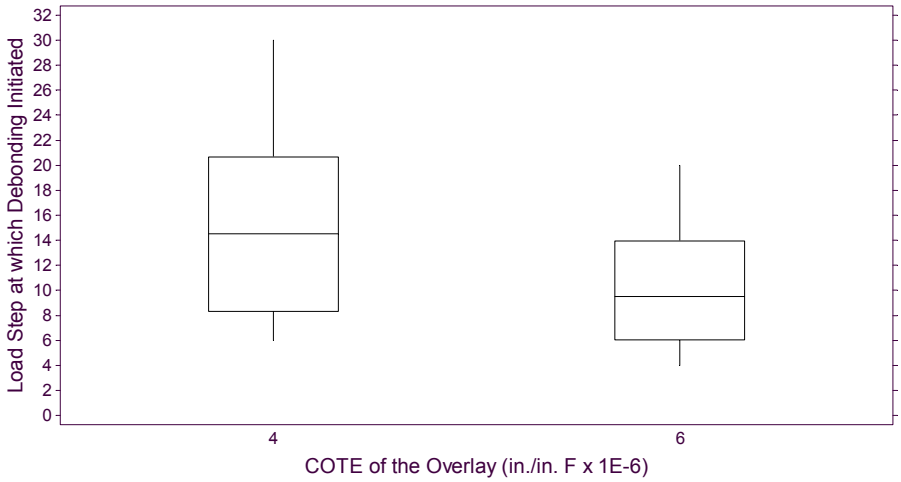

Figure 4.11: Effect of the overlay's CTE on debonding initiation

In addition to significantly increasing the predicted amount of debonding, increases in the CTE of the overlay accelerated the initiation of debonding, as shown in Figure 4.11

In the case of the existing pavement's coefficient of thermal expansion, it is clear from Figure 4.12 and Figure 4.13 that the existing CRCP's CTE does not influence debonding.

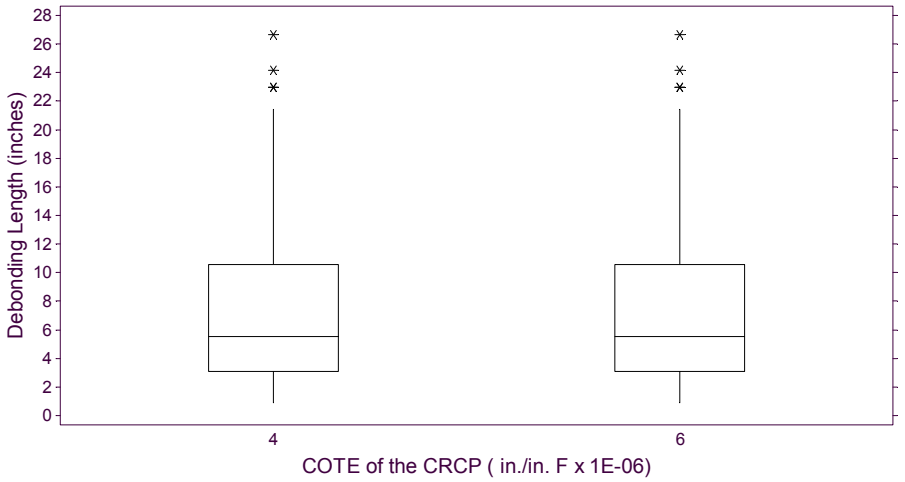

Figure 4.12: Effect of the CRCP's CTE on the predicted amount of debonding length

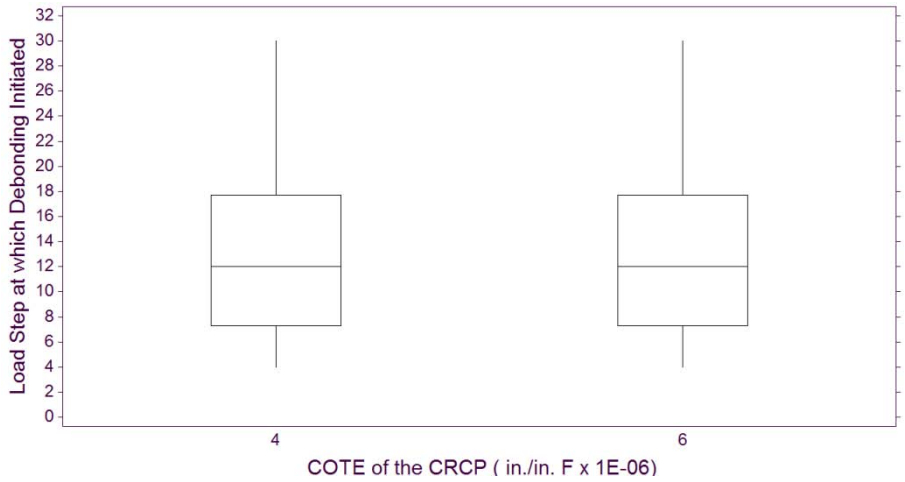

Figure 4.13: Effect of the CRCP's CTE on debonding initiation

4.2.4 Effect of the Modulus of the Overlay

Similarly to the effect brought up by increases in the overlay's CTE, increases in the modulus of the overlay have a moderate impact on debonding initiation and propagation, as shown in Figure 4.14 and Figure 4.15. Note that the use of a concrete mix with a modulus of 5,000,000 psi resulted, on average, in an increase of 2 inches to the 4.2 inches of debonding predicted for an overlay modulus of 4,000,000 psi.

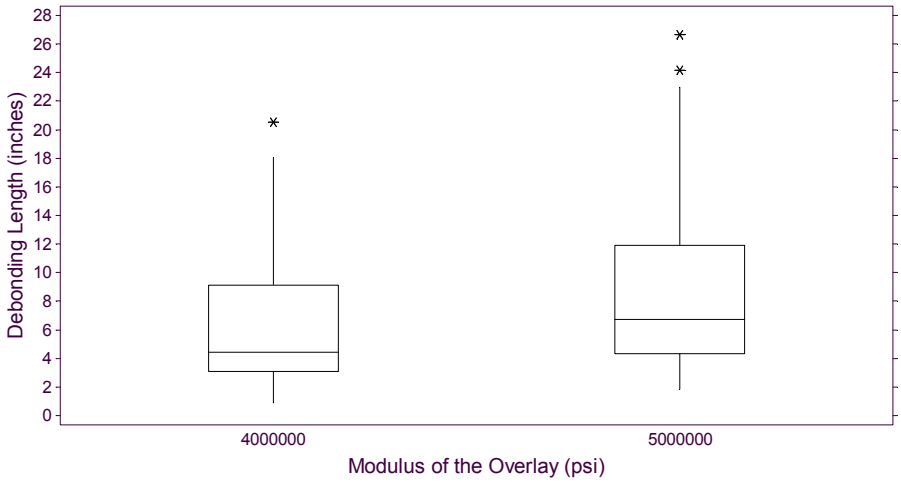

Figure 4.14: Effect of the overlay's modulus on the predicted amount of debonding length

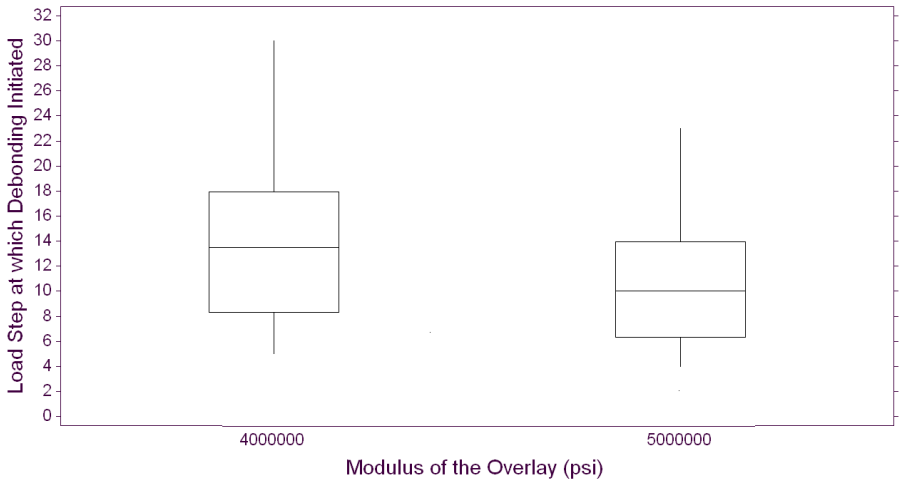

Figure 4.15: Effect of the overlay's modulus on debonding initiation

4.2.5 Effect of the Thickness of the Overlay

As the thickness of the overlay increases, little variation was observed on the predicted amount of debonding, as shown in Figure 4.16. However, for tensile interface strengths of 30 psi, results show that, as the thickness of the overlay increases, the predicted amount of debonding length considerably increases, as shown in Figure 4.17.

Figure 4.16: Effect of the overlay's thickness on the predicted amount of debonding length

Figure 4.17: Effect of the overlay's thickness on the predicted amount of debonding length for low tensile interface strengths

With regards to the influence of the overlay's thickness on the step at which debonding initiated, the results of the sensitivity analysis showed that as the thickness of the overlay increases, the load step at which debonding initiated increased, as shown in Figure 4.18.

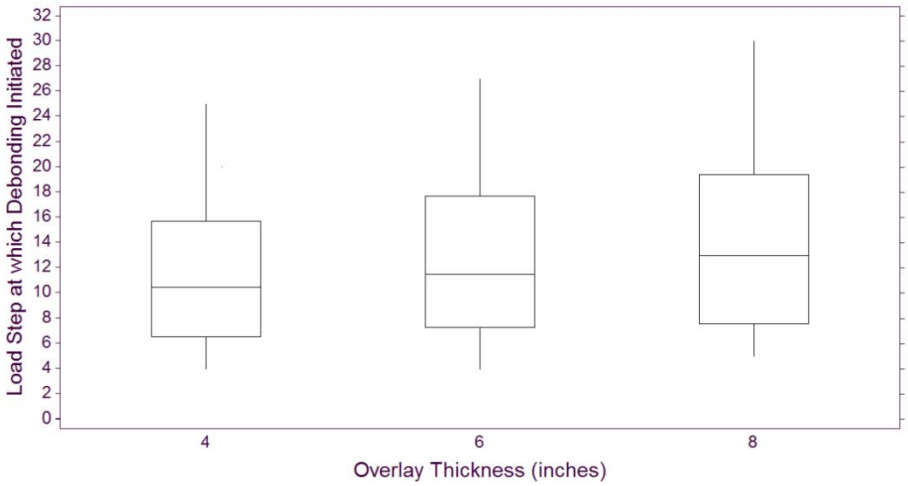

Figure 4.18: Effect of the overlay's thickness on debonding initiation

4.2.6 Effect of the CRCP's Slab Thickness

The results of the sensitivity analysis show that, on average, the thickness of the CRCP slab has little effect on both the predicted length of debonding and the step at which debonding initiated (Figure 4.19 and Figure 4.20, respectively).

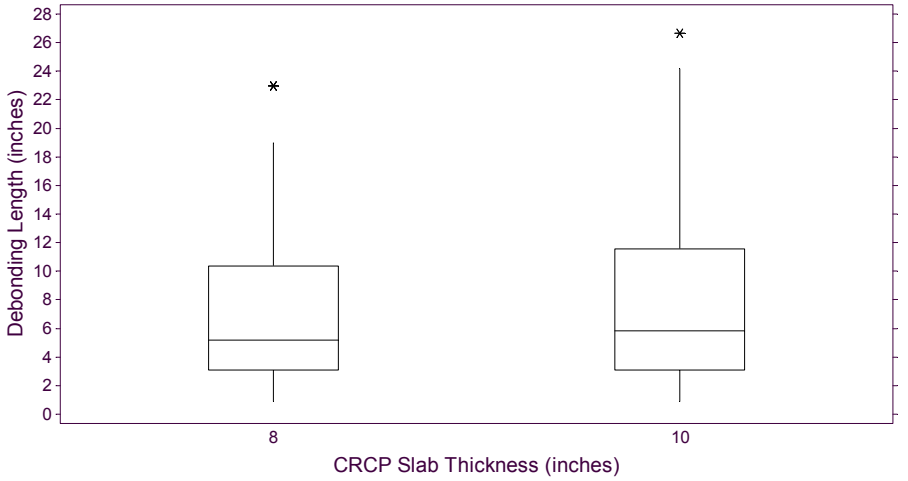

Figure 4.19: Effect of the CRCP's slab thickness on the predicted amount of debonding length

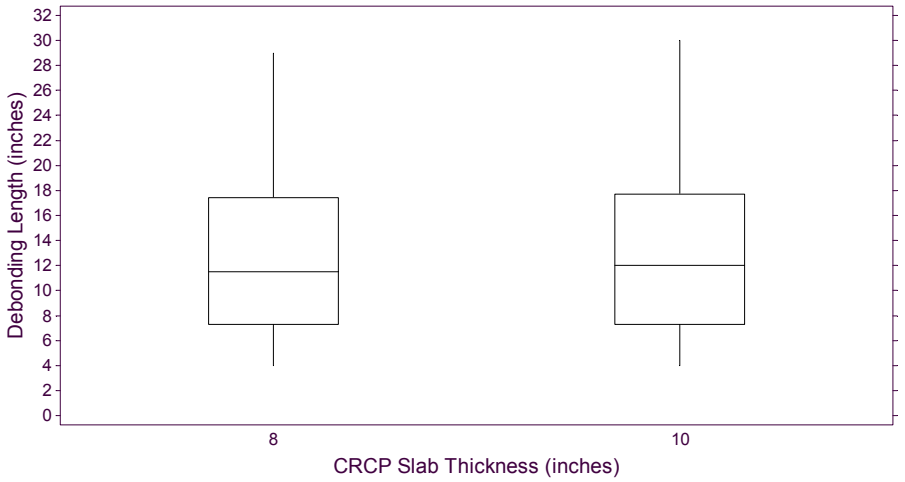

Figure 4.20: Effect of the CRCP's slab thickness on the predicted amount of debonding length

4.2.7 Other Findings

It should be noted that, regardless of the combination of material and geometric properties used for the analysis in this study, in none of the cases analyzed the non-reflective crack induced transverse crack in the existing CRCP.

4.3 Summary

Based on an evaluation of the analysis results, it was demonstrated that the non-reflective crack debonding model is sensitive to the overlay's modulus, the overlay's coefficient of thermal expansion, the overlay's thickness and the interface bond strength. Among the variables that a designer can control, the coefficient of thermal expansion and the overlay's modulus had the most significant effect on debonding. Consequently, among the concrete mix design alternatives considered for resurfacing the existing pavement, priority should be given to mixes that produce low moduli and coefficients of thermal expansion.

For increasing overlay thickness, results showed that, in general, there is little variation in the predicted amount of debonding length for increasing overlay thicknesses. However, for poor bond strength conditions, a considerable increase of debonding lengths could be expected for increasing overlay thicknesses. With regards to the influence of the overlay's thickness on the step at which debonding initiated, the results of the sensitivity analysis showed that thicker overlays delayed debonding initiation to some extent.

Results of all simulations showed that for the typical range of bond strength values, adverse environmental conditions may result in significant amounts of debonding, regardless of the combination of material and geometric properties of the BCO. However, for tensile interface strengths in excess of 300 psi, debonding may be prevented in some cases. Conversely, in order to reduce the potential for debonding to a minimum, special attention should be paid to the preparation of the existing slab surface, as to ensure adequate bond strength.

All other variables, including the existing CRCP's coefficient of thermal expansion and slab thickness had little effect on both the predicted length of debonding and the step at which debonding initiated.

Chapter 5. Conclusions and Recommendations

5.1 Conclusions

The main objective of this study was to develop a mechanistic model capable of determining the extent of debonding for a variety of material, geometric and environmental conditions. To that end, two 2-dimensional finite element models were constructed and the behavior of the BCO was investigated through a sensitivity analysis.

Based on an evaluation of the results provided by the sensitivity analysis, the following conclusions were made:

1. Non-reflective cracks in the overlay will not propagate down into the existing CRCP slab, even in the absence of debonding.
2. Prior to debonding initiation, the maximum interface stresses occur in the vicinity of the non-reflective crack, with the stresses decreasing quickly as we move away from the discontinuity.
3. For the typical range of bond strength values, adverse environmental conditions may result in debonding regardless of the combination of material and geometric properties of the BCO. However, under these circumstances, tensile interface strengths in excess of 300 psi may inhibit debonding initiation.
4. In order to reduce the potential for debonding to a minimum, special attention should be paid to the preparation of the existing slab surface, so as to ensure adequate bond strengths between the overlay and the substrate.
5. The use of aggregates for the overlay's concrete that produce low moduli and thermal coefficient of expansion should improve BCO performance by reducing debonding.
6. Debonding initiation was slightly delayed by increasing overlay thicknesses. However, for poor bond strength conditions, the use of thicker overlays resulted in quite larger debonding lengths.
7. The existing slab thickness and the existing slab coefficient of thermal expansion had little effect on debonding.

5.2 Recommendations for future work

A design tool for BCOs in the form of a computer program can be developed using the model presented herein. Ideally, this tool could assist practitioners in the proper selection of design variables to ensure good early-age behavior for the prevailing environmental conditions. There are, however, some limitations to address in the developed finite element model. In the following paragraphs, some of the aspects of the model worthwhile enhancing will be presented.

As it is, the developed model is to simplistic for practical application. A more accurate, predictive tool for this type of analysis would consider a larger number of factors that affect the early age behavior of the overlay, and include maturity models and temperature differential prediction models to more accurately predict concrete material parameters and the temperature

gradient at several critical times of the overlay's early-age life. It is highly recommended that additional efforts be made to finalize the model in this regard.

The validity of the bond slip relationship used in the development of the model has not been proven. Although it has not been demonstrated, it is expected that the relationship defining the interaction between concrete and reinforcing steel to have significant influence on the BCO behavior. It is, therefore, recommended that further work be done in the determination of a more realistic bond slip relationship.

The ultimate normal slip value used to characterize the interface behavior was selected from literature and its validity is yet to be proven. It is therefore recommended that further work be done in verifying the validity of the assumed parameter value by calibrating it to in-service conditions.

Based on an evaluation of the results gathered for the reflective crack debonding model, it was concluded that, for negative thermal differentials, horizontal cracking will presumably occur at the interface between the overlay's reinforcement and new concrete, instead of at the interface between new and old concrete. It is therefore recommended that further research be conducted to gather data about this failure mode through both field and analytical studies.

Appendix A: Preliminary Study Results

Overlay Thickness	Variable	Units	Temperature Differential (1)	(2)	(3)	(4)
8 inch	Critical Stress Location	--	Top	Top	Top	Bottom
	Maximum Tensile Stress Near the Surface of the Overlay	psi	583	585	589	590
	Maximum Tensile Stress Directly on Top of Existing Crack	psi	260	390	519	650
4 inch	Critical Stress Location	--	Top	Top	Bottom	Bottom
	Maximum Tensile Stress Near the Surface of the Overlay	psi	585	585	589	590
	Maximum Tensile Stress Directly on Top of Existing Crack	psi	294	442	590	737
2 inch	Critical Stress Location	--	Top	Top	Bottom	Bottom
	Maximum Tensile Stress Near the Surface of the Overlay	psi	599	606	618	627
	Maximum Tensile Stress Directly on Top of Existing Crack	psi	312	467	622	779

(1) Bilinear with -28.50 F at the surface of the overlay, -2.85 F at the Interface, and 0.00 F at the bottom of the existing pavement
(2) Bilinear with -28.50 F at the surface of the overlay, -4.28 F at the Interface, and 0.00 F at the bottom of the existing pavement
(3) Bilinear with -28.50 F at the surface of the overlay, -5.70 F at the Interface, and 0.00 F at the bottom of the existing pavement
(4) Bilinear with -28.50 F at the surface of the overlay, -7.13 F at the Interface, and 0.00 F at the bottom of the existing pavement

2 inch Overlay; Thermal Differential (1):

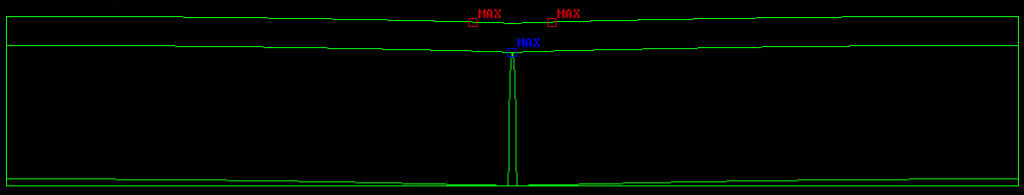

MAX Max. Tensile Stress SXX near the Surface of the Overlay = 4.13 MPa (599 psi)
MAX Max. Tensile Stress SXX Directly on Top of Existing Crack = 2.15 MPa (312 psi)

2 inch Overlay; Thermal Differential (2):

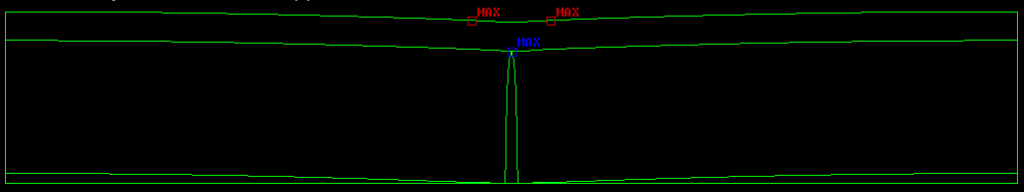

MAX Max. Tensile Stress SXX near the Surface of the Overlay = 4.18 MPa (606 psi)
MAX Max Tensile Stress SXX Directly on Top of Existing Crack = 3.22 MPa (467 psi)

2 inch Overlay; Thermal Differential (3):

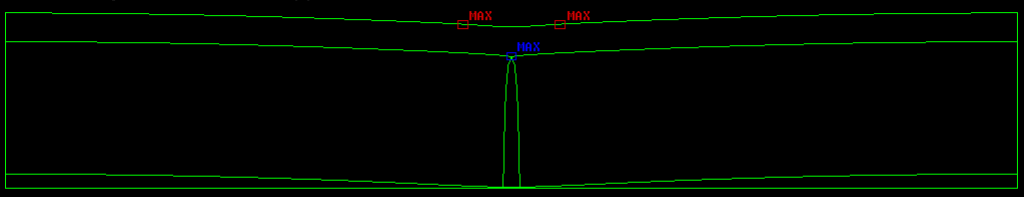

MAX Max. Tensile Stress SXX near the Surface of the Overlay = 4.26 MPa (618 psi)
MAX Max. Tensile Stress SXX Directly above the Existing Crack = 4.29 MPa (622 psi)

2 inch Overlay; Thermal Differential (4):

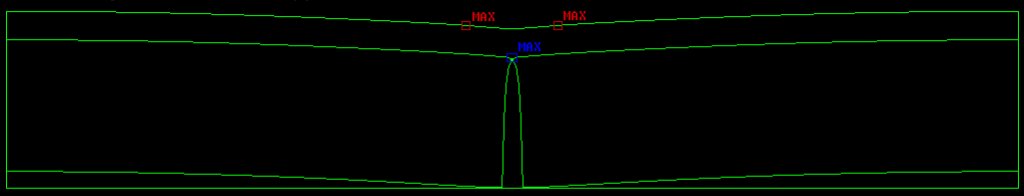

MAX Max. Tensile Stress SXX near the Surface of the Overlay = 4.32 MPa (627 psi)
MAX Max. Tensile Stress SXX Directly on Top of Existing Crack = 5.37 MPa (779 psi)

4 inch Overlay; Temperature Differential (1):

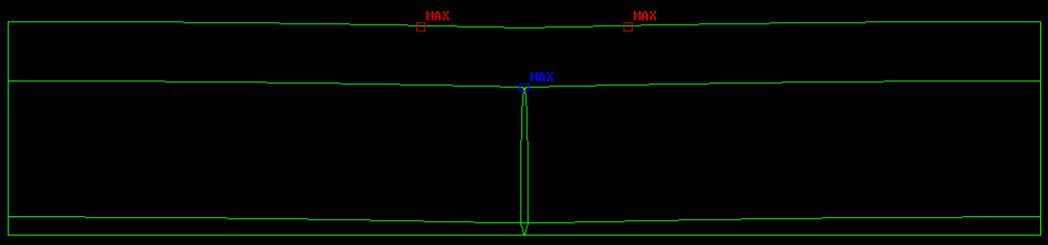

MAX Max. Tensile Stress SXX near the Surface of the Overlay = 4.03 MPa (585 psi)
MAX Max. Tensile Stress SXX Directly on Top of Existing Crack = 2.03 MPa (294 psi)

4 inch Overlay; Temperature Differential (2):

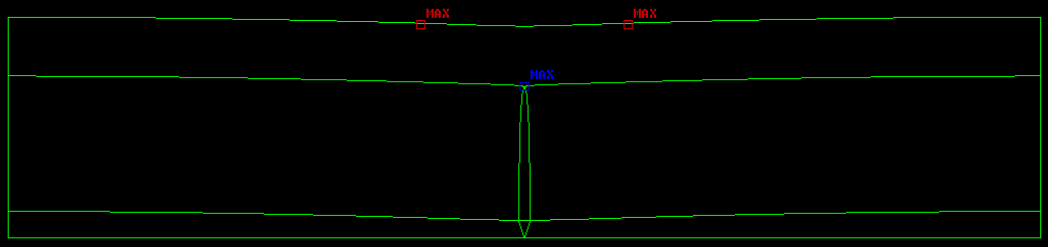

MAX Max. Tensile Stress SXX near the Surface of the Overlay = 4.03 MPa (585 psi)
MAX Max. Tensile Stress SXX Directly on Top of Existing Crack = 3.05 MPa (442 psi)

4 inch Overlay; Temperature Differential (3):

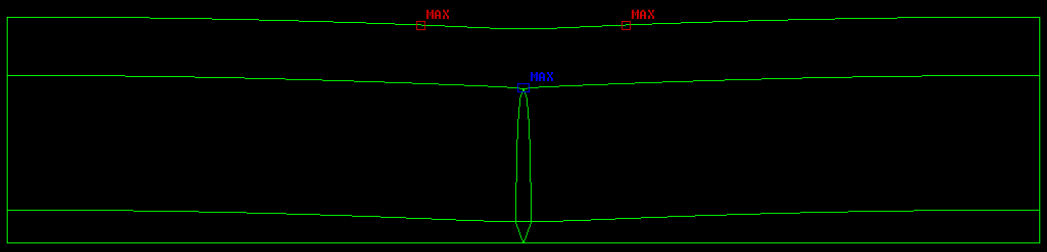

MAX Max. Tensile Stress SXX near the Surface of the Overlay = 4.06 MPa (589 psi)
MAX Max. Tensile Stress SXX Directly on Top of Existing Pavement = 4.07 MPa (590 psi)

4 inch Overlay; Temperature Differential (4):

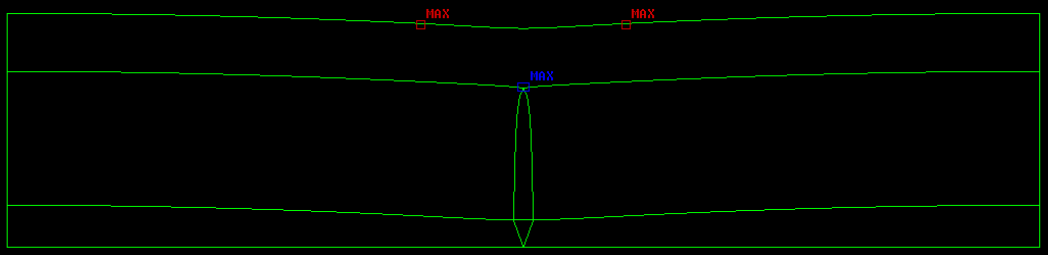

MAX Max. Tensile Stress SXX near the Surface of the Overlay = 4.07 MPa (590 psi)
MAX Max. Tensile Stress SXX Directly on Top of Existing Crack = 5.08 MPa (737 psi)

8 inch Overlay; Temperature Differential (1):

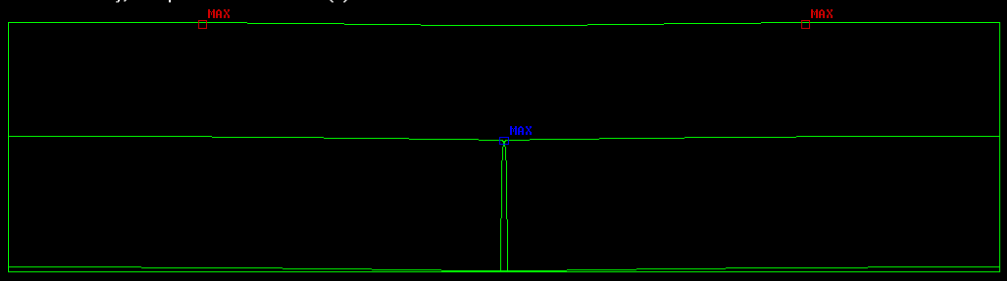

MAX Max. Tensile Stress SXX near the Surface of the Overlay = 4.02 MPa (583 psi)
MAX Max. Tensile Stress SXX Directly on Top of Existing Crack = 1.79 MPa (260 psi)

8 inch Overlay; Temperature Differential (2):

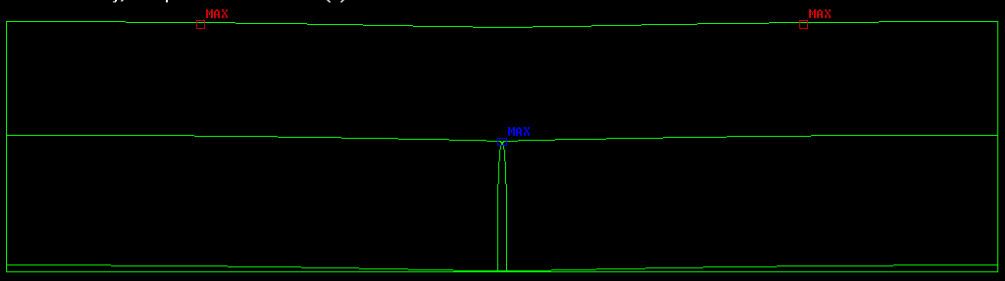

MAX Max. Tensile Stress SXX near the Surface of the Overlay = 4.03 MPa (585 psi)
MAX Max. Tensile Stress SXX Directly on Top of Existing Crack = 2.69 MPa (390 psi)

8 inch Overlay; Temperature Differential (3):

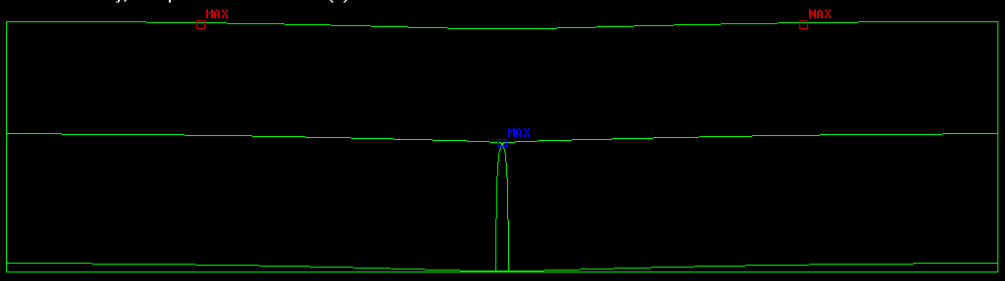

MAX Max. Tensile Stress SXX near the Surface of the Overlay = 4.06 MPa (589 psi)
MAX Max. Tensile Stress SXX Directly on Top of Existing Crack = 3.58 (519 psi)

8 inch Overlay; Temperature Differential (4):

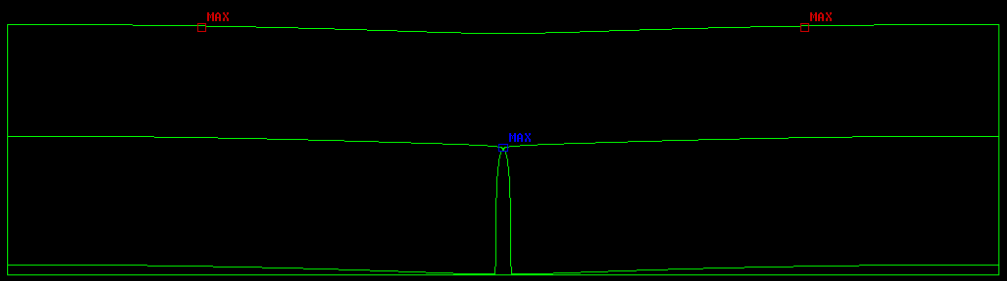

MAX Max. Tensile Stress SXX near the Surface of the Overlay = 4.07 MPa (590 psi)
MAX Max. Tensile Stress SXX Directly on Top of Existing Crack = 4.48 MPa (650 psi)

References

1. Trevino, M, McCullough B. Frank and Fowler, D. W., *"Techniques and Procedures for Bonded Concrete Overlays"*, Research Report 0-4398-2, Center for Transportation Research, University of Texas at Austin, Austin, TX, Feb 2004.

2. Knutson, M. J., *"Iowa's Bonded Portland Cement Concrete Overlays"* Iowa Concrete Paving Association, West Des Moines, IA, November 1977.

3. Neal, B. F., *"California's Thin Bonded PCC Overlay"*, United States Department of Transportation, Federal Highway Administration, Report No. FHWA/CA/TL-83/04, June 1983.

4. Bagate, M., McCullough, B. F., Fowler, D. W., Muthu, M., *"An Experimental Thin-Bonded Concrete Overlay Placement"*, The University of Texas at Austin, Center for Transportation Research, Research Report 357-2F, Nov 1985.

5. Koesno, K, McCullough, B. F., *"Evaluation of the Performance of the Bonded Concrete Overlay on Interstate Highway 610 North, Houston, Texas"*, The University of Texas at Austin, Center for Transportation Research, Research Report 920-2, Dec 1987.

6. Teo, K. J., Fowler, D. W., McCullough, B. F., *"Monitoring and Testing of the Bonded Concrete Overlay on Interstate Highway 610 North, Houston, Texas"*, The University of Texas at Austin, Center for Transportation Research, Research Report 920-3, Feb 1989.

7. Fowler, D. W., McCullough, B. F., *"Bonded Concrete Overlay (BCO) Project Selection, Design, and Construction"*, The University of Texas at Austin, Center for Transportation Research, Research Report 920-6, Nov 1994.

8. Ruiz, J. M., Rasmussen, R. O., Chang, G. K., Dick, J. C., Nelson, P. K., "Computer Based Guidelines for Concrete Pavements, Volume II – Design and Construction Guidelines and HIPERPAV II User's manual", United States Department of Transportation, Federal Highway Administration, Report No. FHWA-HRT-04-122, February 2005.

9. Miller, J. S., Bellinger, W. Y., *"Distress Identification Manual for the Long-Term Pavement Performance Program (Fourth Revised Edition)"*, United States Department of Transportation, Federal Highway Administration, Report No. FHWA-RD-03-031, June 2003.

10. Huang, Y. H., *"Pavement Analysis and Design"*, 2nd Edition, Prentice Hall, 2004.

11. AASHTO 1993, "AASHTO Guide for Design of Pavement Structures", American Association of State Highway and Transportation Officials, Washington DC, 2001.

12. NCHRP I-37, “Guide for Mechanistic-Empirical Design of New and Rehabilitated Pavement Structures”, Part 3, Chapter 4. March 2004.

13. NCHRP I-37, “Guide for Mechanistic-Empirical Design of New and Rehabilitated Pavement Structures”, Appendix LL. July 2003

14. Lundy, J. R., McCullough B. F. and Fowler, D. W., *"Delamination of Bonded Concrete Overlay at Early Ages”*, Research Report 1205-2, Center for Transportation Research, University of Texas at Austin, Austin, TX, Jan 1991.

15. Rots, J. G., *“Computational Modeling of Concrete Fracture”*, Ph.D. Dissertation, Delft University, 1988

16. Rots, J. G., *“Comparative Study of Crack Models”,* Finite Elements in Civil Engineering Applications: Proceedings from the Third DIANA World Conference, Tokyo, Japan, Oct 2002, pp 17-28.

17. Karihaloo, B. L., *“Fracture Mechanics & Structural Concrete”*, Longman Scientific and Technical, Essex, England, 1995

18. DIANA 9, “*User’s Manual”*, TNO DIANA BV, Delft, the Netherlands, 2005.

19. Mehta, P. K., and Monteiro P. J. M., *“Concrete Microstructure, Properties and Materials”*, Prentice Hall, 2001.

20. Neville, A. M., *“Properties of Concrete”*, 4th Edition, John Wiley and Sons, New York, 1996.

21. Mindess, S., Young, J. F., *“Concrete”*, Prentice-Hall, N.J.,2003

22. Bažant Z., P., *“Concrete Fracture Models: Testing and Practice”*, Engineering Fracture Mechanics 69, (2002), 165-205.

23. Delatte, N. J. Jr., Fowler, D. W., McCullough, B. F., *“High Early Strength Bonded Concrete Overlay Design and Construction Methods for Rehabilitation of CRCP”*, Research Report 2911-4, Center for Transportation Research, University of Texas at Austin, Austin, TX, Nov 1996.

24. Granju, J. L., *“Debonding of Thin Cement-Base Overlays”*, Journal of Materials in Civil Engineering”, March/April 2001.

25. Granju, J.L., Sabathier, V., Toumi, A., *“Interface between an Old Concrete and a Bonded Overlay: Debonding Mechanism”*. Interface Science, Volume 12, 2004, pp 381-388.

26. Granju, J.L., *“Debonding of Thin Cement-Based Overlays.”* Journal of Material in Civil Engineering, Volume 13, No. 2, March/April 2001, pp 114-120.

27. Granju, J. L., Toumi, A., Tran, Q. T., *"Experimental and Numerical Investigation of the Debonding Interface between an Old Concrete and an Overlay"*, Journal of Materials and Structures, Volume 39, 2006, pp 379-389.

28. Sadouki, H., Van Mier, J. G. M., "Simulation of Hygral Crack Growth in Concrete Repair Systems", Journal of Materials and Structures, Volume 30, Nov 1997, pp 518-526.

29. Lowes, L. N., *"Finite Element Modeling of Reinforced Concrete Beam Column Bridge Connections"*, Ph.D. Dissertation, University of California, Berkeley, 1999.

30. H. G., Kwak, F. C., Filippou, "Finite Element Analysis of Reinforced Concrete Structures under Monotonic Loads", University of California at Berkeley, 1990.

31. Kim, S-M., Won, M. C., McCullough, D. F., *"Development of a Finite Element Program for Continuously Reinforced Concrete Pavements"*, Research Report 1758-S, The University of Texas at Austin, Center for Transportation Research, Nov 1997.